Applied Catalysis B: Environment and Energy 385 (2026) 126305

Contents lists available at ScienceDirect

Applied Catalysis B: Environment and Energy

journal homepage: www.elsevier.com/locate/apcatb

Role of Mg:Al ratio and Pt promotion on mitigating the deactivation of Ni-based methane steam reforming catalysts

Andrea De Giacinto [a], Enrico Tusini [a,1], Dmitry E. Doronkin [a,b], Solenn Reguer [c], Radian Popescu [d], Jan-Dierk Grunwaldt [a,b], Maria Casapu [a,*]

[a] Institute for Chemical Technology and Polymer Chemistry (ITCP), Karlsruhe Institute of Technology, Engesserstrasse 18, Karlsruhe 76131, Germany
[b] Institute of Catalysis Research and Technology (IKFT), Karlsruhe Institute of Technology, Hermann-von-Helmholtz-Platz 1, Eggenstein-Leopoldshafen 76344, Germany
[c] Synchrotron SOLEIL, L'Orme des Merisiers, Départementale 128, Saint Aubin 91190, France
[d] Laboratory for Electron Microscopy (LEM), Karlsruhe Institute of Technology (KIT), Engesserstraße 7, Karlsruhe 76131, Germany

ARTICLE INFO

Keywords:
Methane Steam Reforming
Ni-based catalysts
Mg:Al ratio
Catalyst deactivation
In situ/operando characterization

ABSTRACT

Ni-based catalysts for CH_4 steam reforming require fine-tuning to withstand deactivation under dynamic operation conditions relevant to emerging H_2-driven technologies. This study investigates the impact of the Mg:Al ratio and Pt presence in catalyst composition on the activity and stability of industrially relevant Ni-based mono- and bimetallic catalysts during simulated daily start-up and shut-down cycles in various gas atmospheres. The evolution of the catalyst structure during extensive testing procedures was investigated in detail by complementary electron microscopy, *in situ/operando* XAS and XRD. The results obtained revealed that catalyst deactivation is promoted at high Mg:Al ratios and especially affects the monometallic catalysts. By converting CH_4 at lower temperatures, Pt regulates the extent of Ni oxidation and its incorporation into MgO lattice. Further prevention of catalyst deactivation was achieved by optimizing the reactor shut-down procedure to minimize the simultaneous exposure to high temperatures and H_2O vapors. By flushing the reactor with N_2 only around the reaction extinction temperature, a fraction of Ni species is maintained in metallic state, which is beneficial for the long-term activity and reaction operation economy.

1. Introduction

The chemical industry needs to undergo a profound transformation as the world attempts to reduce the emission of greenhouse gases (GHG) and approach net-zero targets. In this context, the concept of a hydrogen-based economy has emerged during the last decades, with hydrogen to be exploited both as a raw material for the chemical industry [1–3] and as an energy carrier [4]. Consequently, a constant yearly increase in its demand has been recorded with 100 Mt/year encountered in 2024 and over 2 % increase from 2023 [5]. Generally, hydrogen can be produced by reforming reactions of fossil fuels, which can involve carbon capture, utilization and storage (CCUS). Depending on the reaction path, hydrogen is labeled as gray or blue, with the latter encompassing CCUS [6]. Despite recent efforts for obtaining green hydrogen exclusively based on renewable resources (*e.g.* water electrolysis), the state-of-the-art technologies for the bulk production of hydrogen and syngas (H_2/CO mixtures) remain the catalytic partial oxidation (1) and steam reforming of methane, SRM, (2) reactions with subsequent water-gas-shift, WGS, (3) or their combinations (*e.g.*, autothermal reforming ATR) [3,6,7].

$$CH_4 + \frac{1}{2}O_2 \rightleftharpoons 2H_2 + CO \quad (1)$$

$$CH_4 + H_2O \rightleftharpoons 3H_2 + CO \quad (2)$$

$$CO + H_2O \rightleftharpoons H_2 + CO_2 \quad (3)$$

Currently, the steam reforming of methane (SRM) contributes to over 60 % of the worldwide hydrogen production, with an additional 20 % of hydrogen produced by coal gasification [5]. To maximize methane conversion and achieve optimal cost-performance, SRM relies on steady-state reaction conditions at high temperatures (above 800 °C). The operating temperature and feedstock composition employed are crucial for allowing continuous and economical operation of the reactor

* Corresponding author.
E-mail address: maria.casapu@kit.edu (M. Casapu).
[1] Current address: Stanford Synchrotron Radiation Laboratory, SLAC National Accelerator Laboratory, Menlo Park, CA 94025, USA.

https://doi.org/10.1016/j.apcatb.2025.126305
Received 5 November 2025; Received in revised form 9 December 2025; Accepted 10 December 2025
Available online 15 December 2025

[1]. In particular, based on thermodynamic calculations, no carbon is expected to form at steam to carbon ratios (S:C) higher than 1.2 [1]. The high temperature ensures full conversion and approach to equilibrium at the reformer exit, but in turn promotes the sintering of the active metals.

Because of their cost-effectiveness and high reforming activity, Ni-based catalysts supported on metal oxides (Al_2O_3, MgO, $CaAl_2O_4$ and their mixed oxides) are widely employed for reforming reactions. In these materials, the Ni loading ranges between 15 and 30 wt% [1,8–10]. In order to activate CH_4 during SRM, the presence of metallic Ni is required [1]. Typically, catalyst activation in industrial plants is achieved at high temperatures by feeding a stream of steam and hydrocarbons [1]. As soon as some metallic Ni is available, the steam reforming reaction (Eq. 2) will produce enough H_2 to allow complete catalyst reduction and activation. However, in the long term and depending on the operative conditions (temperature, pressure, feedstock composition), Al_2O_3-supported Ni-based catalysts suffer from deactivation due to sintering and coking, together with possible incorporation of Ni into the support material (*e.g.*, $NiAl_2O_4$) [1,11,12]. As feasible solutions, the addition of magnesium (Mg) and/or noble metals (NMs) into Ni-based catalysts was shown to enhance their long term stability [8–10]. In this regard, catalysts supported on hydrotalcite (HTC)-derived Mg-Al mixed oxides [11,13] or bimetallic catalysts [11,14] have recently attracted much interest. Herein, exploiting the strong interaction between Ni and MgO [15–21] and/or adding small amounts on noble metals (NM) like Pt, Pd, Rh [14] to the Ni-based catalysts improves its resistance toward sintering and coke formation.

Hydrogen production for use in polymer electrolyte fuel cells for auxiliary power units has recently emerged as a promising solution to the fluctuating heat and energy demands in domestic applications [22,23]. However, the current lack of a suitable H_2 delivery infrastructure and the risks associated with H_2 storage at high pressure [24] advocate for pure H_2 production on demand and on site *via* SRM as a viable solution. Nevertheless, in contrast to the common continuous industrial operation, the reactor requires in this case a daily start-up and shut-down (DSS) operation mode, in line with the peaks and pits in power demand. Under such dynamic conditions, steam is normally used as a safety purge gas for idling and coking clean-up [8,25,26], which limits the stability of Ni-based catalysts [25,27]. Instead, the use of inert gas appears as a possible solution. Depending on the required gas purity, this approach could result in additional operating costs. Furthermore, water and/or oxygen traces in the inert gas stream still represent a threat for the catalyst performance. Ohi *et al.* [25] have shown that applying air or steam during the reactor purge, despite being convenient from the technical point of view, results in severe deactivation for monometallic Ni/Mg(Al)O catalysts. The authors related the pronounced activity drop to Ni oxidation and formation of $Mg(OH)_2$, which underlines the importance of tuning the support composition to achieve an optimal metal-support interaction. However, these conclusions mostly rely on *ex situ* characterization of the used catalysts. Considering the dynamic change in catalyst structure under SRM conditions [27], *in situ/operando* studies are especially important when studying catalyst deactivation/reactivation phenomena [25,28–33]. For example, Vogt *et al.* [34] used *operando* infrared (IR) spectroscopy to find experimental descriptors for catalytic activity of Ni/SiO_2 catalysts. Furthermore, Braga *et al.* [35] employed *in situ* XPS to track the surface composition of Ni-Fe/CeO_2 catalysts, and correlated the surface segregation of Fe species with a lower catalytic activity and higher resistance towards coke formation. During reverse water gas shift reaction, Liu *et al.* [36] were able to track the Ni-Pt interaction with *in situ* XAS measurements and understood the alloying dynamics between the two metals. The scarcity of analogous studies in the field of catalytic SRM is most probably linked to the challenges arising from the demanding reaction conditions. Only recently, thanks to the availability of a new *in situ/operando* cell able to reach temperatures up to 1000 °C [37], our group reported on the evolution of Ni species and their interaction with the support material under reaction conditions [27]. Our *operando* XAS investigations showed that the oxidation of Ni and formation of mixed oxides occur to a certain extent in both mono - and bimetallic Ni-based catalysts at low temperatures in the SRM gas mixture due to the presence of water vapor and decreased CH_4 conversion. Such *in situ* and *operando* studies are particularly important in the context of dynamic catalyst operation, where monitoring the structural changes occurring during start-up/shut-down procedures can provide insightful guidelines for knowledge-based catalyst design and the implementation of optimized reactor operation protocols.

In this regard, we report a systematic investigation on the effect of the support composition and reactor purging conditions during dynamic operation mode of mono- and bimetallic Ni or Ni-Pt catalysts supported on HTC-derived Mg-Al oxides. In addition to the effect of Pt promotion on the catalyst activity and durability, the Mg:Al ratio was varied to elucidate its influence on the Ni-support interaction and catalyst deactivation behavior. Various SRM reactor shut-down procedures were simulated (*i.e.*, steam, inert, reaction gas mixture), which are relevant options during the application of small-scale fuel reformers with daily start-up and shut-down operation. Finally, the ability of the mono- and bimetallic catalysts to self-regenerate directly during SRM (S:C=3) without a pre-reductive step was tested, as a necessary prerequisite for their industrial implementation. Beside extensive performance tests, the catalyst structural changes occurring during the SRM light-off, reductive treatment, reactor shutting down and catalyst reactivation steps were monitored by complementary *in situ/operando* X-ray absorption spectroscopy (XAS) and X-ray diffraction (XRD) measurements. The obtained outcome allowed to identify an optimal catalyst composition and prototypical shut-down procedure with minimal effects during long-term application of Ni-based SRM catalysts under dynamic reaction conditions.

2. Experimental methods

2.1. Catalyst preparation

Mg-Al hydrotalcites, commercially available from SASOL GmbH with nominal molar ratios of Mg:Al= 3 (PURAL MG70) or Mg:Al= 0.5 (PURAL MG28), were used as precursors to obtain supports for the mono- and bimetallic Ni–Pt catalysts after calcination at 900 °C for 12 h in static air. Subsequently, incipient wetness impregnation (IWI) was used to synthesize the supported catalysts, employing tetraamine platinum nitrate ($Pt(NH_3)_4(NO_3)_2$) and/or nickel nitrate hexahydrate ($Ni(NO_3)_2{\cdot}6\,H_2O$) as active metals precursors. The bimetallic Ni–Pt catalysts were prepared *via* co-impregnation. The resulting samples were dried at 70 °C for 12 h and afterwards calcined at 500 °C for 5 h in static air (ramp rate 10 °C/min). The nominal metal concentrations in the mono- and bimetallic catalysts were 15 wt% Ni and 1 wt% Pt. Accordingly, the mono- and bimetallic samples are denoted as 15Ni/MGXX and 15Ni1Pt/MGXX, respectively. XX= 28 represents MG28 (Mg:Al=0.5) and XX= 70 represents MG70 (Mg:Al=3) supports, depending on the hydrotalcite used to obtain the carrier material.

2.2. Catalyst characterization

The specific surface area of the samples was determined by N_2 physisorption at −196 °C using a BELSOPRP-mini instrument (MicrotracBEL, Osaka, Japan) and according to the Brunauer–Emmett–Teller theory [38]. The samples were degassed at 200 °C for 2 h in vacuum before the analysis and the adsorption isotherms were evaluated in the range of $p/p_0 = 0.05–0.3$.

The crystallinity of the materials was assessed *via* X-ray diffraction (XRD) using a D8 Advance (Bruker) diffractometer using Cu Kα radiation (λ=1.5406 Å). The patterns were recorded between 10° and 120° 2θ using a step size of 2θ= 0.017° and 10 s per step dwell time.

Temperature-programmed reduction with H_2 (H_2-TPR) was performed on an AutoChem II instrument (Micromeritics, Norcross, USA)

by heating the calcined sample (45 ± 5 mg of 125–250 μm sieved fraction) from room temperature (25 °C, RT) to 900 °C with 10 °C/min heating rate while dosing 50 mL/min of 10 vol% H_2/Ar. Before the reduction step, adsorbed species were removed by heating the sample in 50 mL/min of 10 vol% O_2/He from RT to 500 °C (15 min holding time). The H_2 consumption was monitored using a thermal conductivity detector (TCD).

For all catalysts, Ni, Pt, Mg and Al metal loadings were determined by inductively coupled plasma optical emission spectroscopy (ICP-OES) using an OPTIMA 4300 DV spectrometer (PerkinElmer, Waltham, USA). 30 ± 0.05 mg of the samples was dissolved in 4 mL hydrochloric acid, 4 mL sulfuric acid and 2 mL hydrogen peroxide at 250 °C for 1 h in the XPERT microwave digestion system (Berghof). The analysis of the elements was accomplished with four different calibration solutions and an internal standard (Sc). The range of the calibration solutions did not exceed a decade. Three wavelengths of the elements were used for the calculations.

High-angle annular dark-field (HAADF) scanning transmission electron microscopy (STEM) imaging combined with energy dispersive X-ray spectroscopy (EDXS) was used to investigate the particle size distributions and the elemental distributions of Ni, Mg, Al and Pt (when present) in all the catalysts. The investigations were performed on a FEI Osiris ChemiSTEM microscope at 200 keV electron energy, equipped with a Super-X EDXS system comprising four silicon drift detectors. The particle size distribution was determined based on the evaluation of ~300 nanoparticles (maximum Feret Diameter) using the software ImageJ (version 1.54p) [39]. Concentration profiles of different chemical elements within single nanoparticles were determined after the quantification of EDXS spectra measured along a line-scan that passes through their center (EDXS line scans). EDXS line scans were quantified with the FEI software package "TEM imaging and analysis" (TIA) version 4.7 SP3. The EDXS maps were analyzed by using the ESPRIT software (version 2.3) from Bruker. The ure of Ni-Pt nanoparticles was investigated by high-resolution (HR) transmission electron microscopy (TEM). The measurements were performed on an aberration-corrected FEI Titan^3 80–300 microscope at 300 keV electron energy. HRTEM images were evaluated by calculating the two-dimensional Fourier transform (FT), which yields information on the crystal structure (lattice parameters and crystal symmetry) of single nanoparticles. The analysis was performed by comparing the experimental FT and the calculated diffraction patterns with Miller indices, with the latter obtained by using the Jems electron microscopy simulation software [40].

Raman spectroscopy measurements were conducted with an inVia Reflex Spectrometer System (Renishaw) equipped with a He–Ne laser (633 nm, 17 mW) and an optical microscope (Leica). The data was collected in a spectral range from 130 to 3470 cm^{-1}, with a resolution of 3 cm^{-1} by means of a 600 lines/mm grating, using 10 % laser power and 100 s acquisition time. Data treatment, including cosmic ray removal, noise filtering and baseline subtraction, was done with the software WiRE 4.4 (Renishaw).

2.3. Catalytic tests

Systematic catalytic tests were performed for all the catalysts in a plug flow microreactor. A high temperature cell, previously reported by Eggart *et al.* [37], was used for these experiments. 5 mg of catalyst (sieve fraction 100–200 μm) was loaded into a quartz capillary of 1.5 mm diameter (wall thickness 0.02 mm). The sieve fraction was chosen to minimize mass-transport limitations and ensure low pressure drops in the microreactor. As a first step, the catalysts underwent a prereduction treatment for 1 h at 900 °C (5 vol% H_2/N_2, 50 mL/min total flow, ramp rate 10 °C/min). Afterwards, the reaction mixture (RM: 6600 ppm of CH_4, 2 vol% H_2O in N_2; 50 mL/min total flow) was dosed over the catalyst bed using mass flow controllers (Bronkhorst) and a water vapor gas saturator (kept at room temperature, RT) at a weight hourly space velocity (WHSV) of 10^6 $mL \cdot g^{-1}_{catalyst} \cdot h^{-1}$. This steam to carbon ratio of 3 was chosen to avoid carbon deposition during the catalytic tests. The gas atmosphere during the switches was changed using a motorized four-way valve (VICI Valco Instruments). For catalyst degreening, the reactor was kept at 900 °C under RM for 2 h. Next, the reactor was cooled down to room temperature (RT) under different atmospheres, namely: a) RM; b) N_2; c) H_2O-saturated N_2; d) RM until 600 °C, then switched to N_2 until RT. The cooling ramp rate was of 10 °C/min. To evaluate the catalyst regeneration ability, the RM was dosed again in the reactor and the catalyst was heated with 10 °C/min to 900 °C (light-off), with 5 min holding time. The cooling ramp was also performed in RM (light-out). Supplementary catalyst stability evaluation tests were performed by simulating several start-up/shutdown cycles during four consecutive days of operation. During the first 24 h, after activation for 1 h at 900 °C (5 vol% H_2/N_2, 50 mL/min total flow, the catalyst was exposed to RM at 900 °C for 8 h and subsequently cooled down to RT in N_2 (50 mL/min). For each of the following three days, the start-up procedure consisted in heating up the reactor in RM to 900 °C and holding this temperature and reactor gas feed for 8 h. At the end of each day, the reactor was cooled down to RT in N_2. Between the shut-down/start-up cycles, the reactor was kept in N_2 overnight. The applied heating/cooling ramps were of 10 °C/min. During the whole testing procedure, the outlet gas composition was monitored with a quadrupole mass spectrometer (Pfeiffer Vacuum, Omnistar GSD 320) and an online Fourier transform infrared spectroscopy (FTIR) gas analyzer (MultiGas 2030, MKS Instruments). The onset temperature (T_{onset}) was defined as the point where the auxiliary line through the rising edge of the $m/z = 2$ (H_2) signal from the mass spectrometer (MS) intersects the linearly extrapolated baseline, while the temperatures corresponding to 50 % and 90 % CH_4 conversion (T_{50} and T_{90}) were extracted from the data obtained by the FTIR spectrometer. The CH_4, CO, and CO_2 equilibrium concentrations at 1 atm and different temperatures (100–900 °C) were calculated by solving both SRM and WGS reactions equilibria in an iterative way using the inlet gas composition as starting concentrations. Equilibrium constants were taken from Hou *et al.* [41].

2.4. In situ and operando X-ray absorption spectroscopy (XAS)

The *in situ/operando* XAS measurements were performed at the P65 beamline of the PETRA III synchrotron (DESY, Hamburg, Germany). Energies of the incident X-rays were selected *via* a water-cooled Si (111) double crystal monochromator. The Ni K (8333 eV) and Pt L_3 (11564 eV) edges were continuously monitored during the same experiment for the bimetallic catalysts, alternating the scans between the two edges. Ion chambers were used to collect the data in transmission mode at Ni K edge, while a passivated implanted planar silicon (PIPS) detector was used to record the fluorescence at Pt L_3 edge. During the whole experiment, the middle of the catalyst bed was monitored with a beam size of about 0.3 mm × 1.5 mm (V × H). For energy calibration, reference XAS spectra of Ni and Pt metal foils were recorded simultaneously with the catalyst data. Data evaluation, including energy calibration and normalization, was performed using Athena and Artemis software from the IFEFFIT software package [42]. For the linear combination fitting (LCF) of the XANES region, the normalized spectra were analyzed in the region −30 eV to + 50 eV around both edges. Spectra of Ni and Pt foils, together with NiO and PtO_2 pellets (both obtained from commercial chemicals) were used as references. As an additional reference for $NiMgO_X$, a 15 wt% Ni/MgO sample obtained by incipient wetness impregnation and calcination at 550 °C (ramp rate 10 °C/min) for 5 h was used. The extended X-ray absorption fine structure (EXAFS) data $\chi(k)$ collected at room temperature were background subtracted, and subsequently analyzed in the *k*-space range of 3–14 $Å^{-1}$ for Ni K edge, and 3–11 $Å^{-1}$ for the Pt L_3 edge. For the fitting of the Ni K edge, the region between 1.0–3.2 Å was selected in the Fourier-transformed (FT) *R*-space data for the calcined samples, while the 1.0–3.0 Å range was used for the reduced samples. For the Pt L_3 edge, the region between

1.0–2.2 Å was used for the calcined samples, while 1.0–3.0 Å was used for the reduced samples. The amplitude reduction factor (S_0^2) estimated from the foil fitting was 0.76 for Pt and 0.80 for Ni. At the Ni K edge, the Ni *fcc* structure (ICSD 37502) was used to model the metallic Ni–Ni shell. $NiMgO_X$ mixed oxide (ICSD 13774) was used for evaluating the formation of a Ni–Mg bond and track the metal-support interaction, while the Ni–O and Ni–Ni scattering paths were modeled based on NiO structure (ICSD 9866). At Pt L_3 edge, the Pt-O scattering path was modeled from PtO_2 (ICSD 202407), while the Ni–Pt interaction was modeled using a NiPt alloy structure (ICSD 105318). Coordination numbers (CN), mean square deviation of interatomic distances (σ^2), interatomic distances (R), and energy shift (ΔE_0) were refined as parameters during the fit. The overall misfit between data and fitting was obtained *via* the R factor. The number of free parameters used for all the fits is below the maximum number according to the Nyquist criterion [43].

For the *in situ/operando* experiments, 5 mg of catalyst (sieve fraction 100–200 μm) was loaded into a quartz capillary of 1.0 mm diameter (wall thickness of 0.02 mm, WJM-Glas Müller GmbH). A hot gas blower (FMB Oxford, UK) was used to heat the capillary reactor. The procedure, reductive and reaction gas mixtures (RM) were identical to those applied during the laboratory catalytic tests, with the exclusion of the last cooling ramp that was performed in He at the beamline instead of RM In a first step, the catalysts underwent a prereduction treatment while continuously collecting XANES spectra to monitor the variations in Ni and Pt (when present) structure. Afterwards, the reaction mixture was dosed into the reactor at a WHSV of 10^6 $mL \cdot g_{catalyst}^{-1} \cdot h^{-1}$ (comparable to the lab scale experiments). The catalyst was kept at 900 °C under RM for 2 h. Afterwards, the methane flow was set to 0 mL/min and He dosage *via* water saturator was increased to keep a total flow of 50 mL/min in the reactor. The reactor was then cooled down to RT (25 °C) in H_2O-saturated inert atmosphere with a cooling rate of 10 °C/min. Lastly, the RM was dosed again in the reactor and the catalyst was heated with 10 °C/min to 900 °C, with 10 min holding time. Afterwards, the gas atmosphere was changed from RM to inert (50 mL/min He) using the motorized four-way valve (VICI Valco Instruments) before cooling down the sample to RT with a cooling rate of 10 °C/min. During the whole testing procedure, the outlet gas composition was monitored with a quadrupole mass spectrometer (Pfeiffer Vacuum, Omnistar GSD 320) and an online FTIR gas analyzer (Gasmet, DX4000).

2.5. *In situ and operando X-ray powder diffraction*

In situ/operando X-ray diffraction experiments were conducted at the DiffAbs beamline of the SOLEIL Synchrotron (Saint-Aubin, France) using a procedure and setup identical to those applied for the *in situ/operando* XAS measurements. The energy selected for the XRD data collection was 8.2 keV, selected using a double Si(111) crystal monochromator and two Rh-coated mirrors. During the experiment, the middle of the catalyst bed was monitored with a beam size of about 0.25 mm × 0.3 mm (V × H). A Circular Hybrid Pixel Array Detector (CirPad) was used [44], which consists of 20 XPAD modules assembled together in a circular arch geometry. The angular range of each acquisition was 4.5–140° 2θ, the angular opening was 0.0115° 2θ and the acquisition time was 30 s per 2D image. While continuously acquiring 2D images, the angular position of the detector (δ angle) was alternated from δ= 0° to δ= 0.5° with an image taken at each angle. By using a Python script implemented at the beamline, each image was individually converted to a diffractogram (intensity vs 2θ) and a background correction for each XPAD module was applied. The obtained diffractograms were merged in groups of 2 (consecutive, δ=0° and δ=0.5°) to retrieve the final diffractograms. The last step was done to eliminate dead zones in between the XPAD modules.

3. Results and discussion

3.1. *Structural features of the as prepared catalysts*

After calcination of the PURAL precursors, nanocrystalline and porous support materials were obtained (Fig. 1a and S1). The XRD reflections of MgO (ICSD 9863) and $MgAl_2O_4$ (ICSD 31373) could be identified in both supports and corresponding catalysts, with different relative intensities. Indeed, in agreement with the nominal Mg:Al ratio of the parent hydrotalcites, MgO represents the dominant crystalline phase of MG70 while $MgAl_2O_4$ is the principal component of MG28 after calcination at 900 °C for 12 h. Despite the nominal Mg:Al ratio of PURAL MG28 corresponding to the stoichiometric $MgAl_2O_4$ mixed oxide, the support obtained after calcination also showed minor reflections from the MgO phase indicating the presence of both species. Nevertheless, the very broad MgO reflections compared to the ones measured for the support derived from MG70 indicate significantly different crystallite sizes of MgO domains. More specifically, smaller MgO crystallites are formed in the support derived from the MG28.

Table 1 summarizes the results obtained by ICP-OES analysis and N_2 physisorption for the four synthesized catalysts. In all mono- and bimetallic samples, the nominal Mg:Al ratio of the hydrotalcite precursor was maintained, yielding two catalysts with Mg:Al= 0.5 (MG28) and two catalysts with Mg:Al= 3 (MG70). The actual metal loadings are in the range 10.4–13.3 wt% for Ni and around 0.83 wt% for Pt, which result in a Ni:Pt molar ratios of 43–48 (large excess of Ni) in the bimetallic samples. The corresponding Ni:Mg molar ratios are 1:3 and 1:6 for the catalysts supported on MG28 and MG70, respectively.

Ex situ XRD measurements conducted for the calcined catalysts also showed reflections that can be ascribed to NiO (ICSD 9866). Due to the isostructural nature and comparable lattice parameters, NiO and MgO exhibit similar crystallographic properties, which prevented quantification of the relative amounts based on the obtained XRD patterns. Nevertheless, when comparing the XRD of the bare supports (Figure S1a) and the XRD of the corresponding calcined Ni-based catalysts (Fig. 1a), a general increase in the intensity of the reflections matching both MgO and NiO can be noticed for all samples. This variation can only be correlated with the formation of either NiO or mixed $NiMgO_X$ entities during the catalyst calcination [15,18,27]. At high angles, the diffraction peaks of NiO, MgO and $NiMgO_X$ are easier to disentangle [45,46]. In particular, the (420) reflection of MgO (2θ = 109.55°) is expected to shift to slightly higher angles when Ni^{2+} ions diffuse into its lattice, while the (420) reflection of pure NiO is expected at (2θ = 111.08°). For both catalysts supported on MG70, the (420) reflection appeared at 2θ = 110.4°, advocating for the formation of $NiMgO_X$ entities. In contrast, for the catalysts supported on MG28 only a diffraction peak at 2θ = 111.3° could be observed, which results from the convolution of the (420) reflection of NiO and the (751) reflection of $MgAl_2O_4$ (Figure S2). Concerning the presence of metallic phases, after

Table 1
Specific surface area (SSA) and elemental analysis of the samples investigated in this study.

Sample	SSA (m^2/g)*	Ni (wt %)**	Pt (wt %)**	Mg (wt %)**	Al (wt %)**	Mg:Al (mol/mol)	Ni:Pt (mol/mol)
15Ni/MG28	80	10.4 ± 0.2	-	13.1 ± 0.4	29.4 ± 1.0	0.49 ± 0.02	-
15Ni/MG70	74	13.3 ± 0.3	-	30.9 ± 1.0	11.0 ± 0.3	3.12 ± 0.13	-
15Ni1Pt/MG28	72	10.5 ± 0.2	0.82 ± 0.02	13.1 ± 0.3	30.1 ± 0.7	0.48 ± 0.02	42.6 ± 1.3
15Ni1Pt/MG70	68	12.0 ± 0.2	0.84 ± 0.02	32.0 ± 0.8	11.9 ± 0.3	2.99 ± 0.11	47.5 ± 1.4

* Determined by N_2 physisorption of the pre-reduced catalyst. ** Determined by ICP-OES for the calcined catalyst.

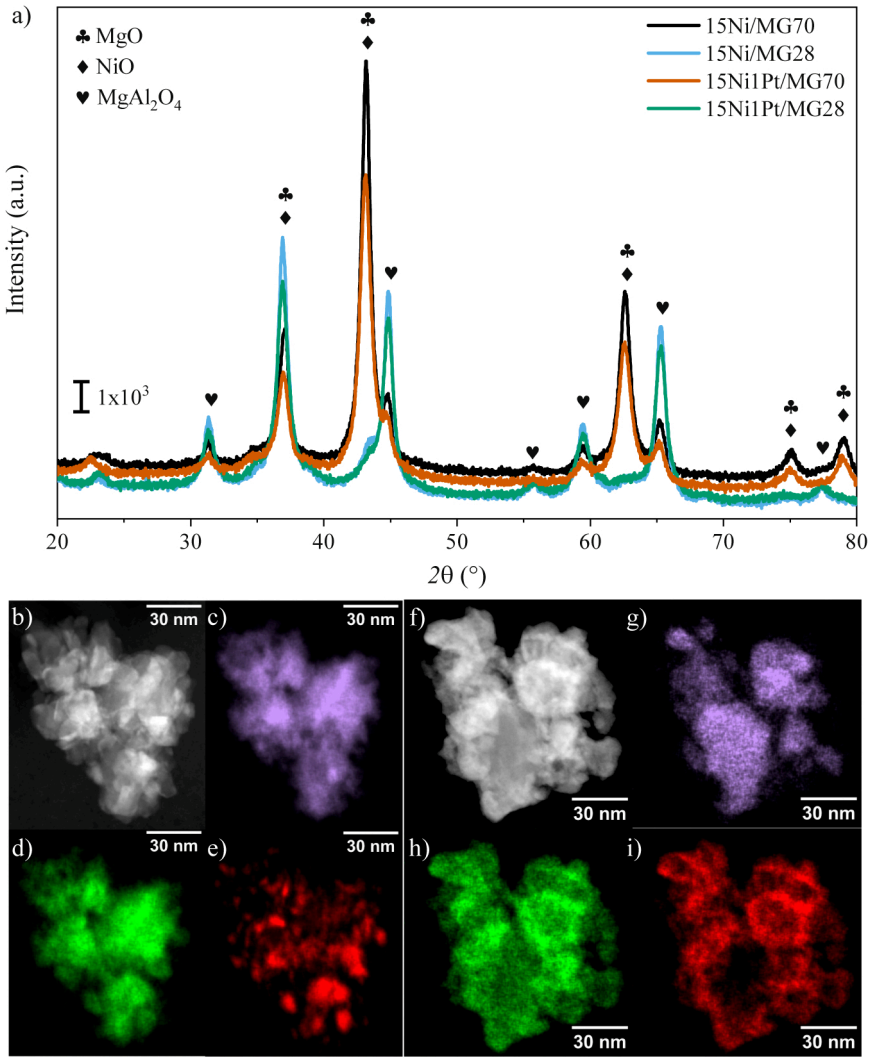

Fig. 1. (a) XRD patterns (λ = 1.5406 Å) of the as prepared (after calcination) catalysts. HAADF-STEM images of (b) 15Ni/MG28 and (f) 15Ni/MG70 in the calcined state. Corresponding EDXS elemental maps for Al (Al-K line, purple, c, g), Mg (Mg-K line, green, d, h) and Ni (Ni-K line, red, e, i).

the calcination step at 500 °C no reflections from reduced Ni or Pt species could be identified, as previously reported for similar systems [27].

To trace the distribution of Ni, Mg, and Al species in the as prepared monometallic catalysts with different Mg:Al ratios, HAADF-STEM and EDXS investigations were additionally performed. As reported in Fig. 1b-i, on the support with a higher Mg:Al ratio (*i.e.* MG70) the overlap of the spatial distributions (obtained by EDXS mapping) of Ni and Mg suggests that the Ni-Mg interaction is promoted in this sample due to the large excess of MgO [15,17]. Furthermore, the X-ray characteristic intensity of the Ni-K line in the corresponding EDXS maps is substantially lower in the Al-rich regions, *i.e.*, supposedly the regions where the $MgAl_2O_4$ phase is present. For the support comprising a lower Mg:Al ratio (*i.e.* MG28), the formation of Ni aggregates of various sizes (5–15 nm) was noticed, with only minor correlations between Ni and Mg locations.

To further assess the local structure of Ni in the as prepared catalysts, *ex situ* XAS data were collected for the catalyst pellets. The XANES region of Ni K edge is reported in Figure S3a. All spectra show similar white line intensity to that displayed by the 15Ni/MgO reference. Nevertheless, above ca. 8356 eV the spectrum profile of 15Ni/MG28 is different in comparison to those measured for the other catalysts, resembling more the shape of the NiO reference. As a next step, linear combination fitting (LCF) was performed for the XANES region (Figure S3b), confirming the visually identified trends regarding the presence of both NiO and $NiMgO_X$ species in all catalysts. The corresponding FT-EXAFS data are reported in Figure S3c, while the fitting results are displayed in Table S1-S3 and Figure S4-S5. The first coordination shell at 2.09 Å with a refined coordination number (CN) of 6 for all samples corresponds to Ni in octahedral coordination geometry with 6 oxygen atoms. This cross-confirms the highly oxidized state of Ni species in all calcined samples, in line with the results derived from the LCF analysis of the XANES region. The second coordination shell at 2.95 Å was found to be represented by the Ni-Mg bond of a $NiMgO_X$ reference structure (details in the experimental section and in the SI). Despite the second coordination shell is expected to involve 12 atoms in a mixed oxide, the results from the fitting were below 8 for all investigated samples, suggesting a relatively small size or flattened shape [47] for Ni-containing particles. Interestingly, the 15Ni/MG28 sample showed the lowest CN for the Ni-Mg path (4.5 ± 1.2) among the investigated catalysts, which is in line with the different spectral features resembling more the NiO reference. This suggests a limited incorporation of Ni in the mixed oxides for this particular sample. Combining these results with the electron microscopy and XRD data, considerable incorporation of Ni^{2+} ions into bulk $NiMgO_X$ was identified on the MG70 support, while only a minor surface incorporation of Ni^{2+} ions into MgO was observed on the MG28 support.

To elucidate the local structure of Pt in the bimetallic catalysts, *ex*

situ XAS data were collected for the catalyst pellets at the Pt L_3 edge. The XANES region is reported in Figure S6a. The obtained spectra show similar profiles to that displayed by the PtO_2 reference, indicating a highly oxidized state of Pt after catalyst calcination. The corresponding FT-EXAFS data are reported in Figure S6b. The fitting results are reported in Table S4-S6 and Figure S7. The first coordination shell at 2.0 Å with a calculated CN of 6 for both bimetallic Ni-Pt samples corresponds to the Pt-O bond in the PtO_2 structure. The absence of pronounced features above 2.0 Å suggests a poor interaction with Ni after calcination and formation of relatively small entities. No features resembling reduced Pt were observed, cross-confirming the highly oxidized state of the noble metal that was also indicated by the analysis of the XANES region. The results obtained in this study on the oxidation states of Ni and Pt species in the catalysts supported on Mg-Al mixed oxides are in line with previous XAS investigations of similar bimetallic samples [27].

To assess the redox behavior of the formed Ni and Pt species and confirm the location of Ni^{2+} ions, H_2-TPR measurements were conducted (Figure S8) in a next step. The profiles of the recorded TCD signal show clear differences in catalyst reducibility depending on their composition. In general, three regions can be assigned to the reduction of Ni species, namely: (i) a low-temperature region from 300 to 500 °C, (ii) an intermediate region from 500 to 750 °C, and (iii) a high temperature region above 750 °C. These ranges were previously assigned to the reduction of: (i) NiO particles on the catalyst surface, having weak interactions with the support [46], (ii) Ni^{2+} ions in the outermost layer and subsurface of Ni-Mg mixed oxides [18,46], and (iii) hardly reducible bulk $NiMgO_X$ mixed oxides [15,17,46]. In comparison, the reduction of bulk NiO occurs between 300 and 450 °C [45,48].

For the two catalysts supported on MG28, the maximum reduction rate of Ni species, given by the highest intensity of the TCD signal, occurred at approx. 560 °C and 515 °C for the mono- and bimetallic catalysts, respectively. At the same time, a broad shoulder was observed at lower temperatures, *i.e.*, ~375 °C (Ni monometallic) and ~345 °C (Ni-Pt bimetallic). Finally, a shoulder is visible around 770 °C (Ni monometallic) and 700 °C (Ni-Pt bimetallic). These multiple reduction peaks indicate the simultaneous presence of NiO-like NPs having a weak interaction with the support material, together with Ni^{2+} ions in the outermost layer and subsurface of mixed oxide phases [45] on the MG28 support. Notably, most Ni species supported on MG28 are reduced up to 750 °C even for the monometallic catalyst. The overall trends indicate moderate diffusion of Ni^{2+} ions in the bulk of mixed oxides as well as a modest impact of the noble metal presence on the reducibility of Ni species, due to its relatively low loading.

Also, for the corresponding catalysts supported on MG70 three distinct reduction regions can be distinguished. However, the reduction peaks in the TCD signal are shifted towards higher temperatures compared to the previous catalyst series. These profiles confirm the stronger interaction of Ni with the support if a higher Mg:Al ratio and a large excess of MgO are used during catalyst synthesis [15,27]. In particular, reduction peaks around 450 °C, 660 °C and 840 °C are visible in the TCD profile of the monometallic 15Ni/MG70 catalyst. Therefore, the reduction of the respective Ni species occurs at temperatures approximately 100 °C higher than those observed for the equivalent monometallic catalyst on MG28. On the other hand, the corresponding bimetallic 15Ni1Pt/MG70 catalyst exhibits reduction peaks at 440 °C, 575 °C and 820 °C in the TCD profile, confirming that also in this case Pt presence slightly promotes the reduction of Ni species.

Overall, the results of the H_2-TPR experiments indicate that the Ni-Mg interaction can be regulated by the support composition, as also highlighted by the HAADF-STEM, EDXS, XRD and XAS investigations of the calcined catalysts. Furthermore, regardless of the support type (MG28 or MG70), the presence of Pt only slightly improved the reducibility of the Ni^{2+} species in the bimetallic samples. For the bimetallic Ni-Pt catalysts, an additional peak between 150 and 250 °C was observed, which could be ascribed to the reduction of Pt species [27]. The higher reduction temperature observed for the 15Ni1Pt/MG70 in this temperature range could be related to the stronger interaction between Pt and MgO, which was previously reported in literature [49–51].

3.2. Generation of active species by catalyst pre-reduction

In order to activate CH_4 during steam reforming, the presence of reduced Ni is required [1]. Indeed, numerous studies that previously investigated Ni-based catalysts applied a reductive pretreatment (normally in H_2 atmosphere) [25,31,33] to generate the active species before feeding the reaction mixture to the reactor and proceeding with the catalytic tests. For these reasons and based on the H_2-TPR results described above, all investigated catalysts were pre-reduced for 1 h in 5 vol% H_2/N_2 at 900 °C. This procedure also helped to stabilize the catalysts towards thermal sintering, as SRM is normally performed at temperatures well above the Tammann temperature of nickel (ca. 590 °C) [1].

The measured specific surface area (SSA) of the pre-reduced catalysts is in the range of 70–80 m^2/g, as reported in Table 1. The *ex situ* XRD patterns collected for the pre-reduced catalysts are shown in Fig. 2a. The presence of Ni fcc (ICSD 37502) reflections confirmed the formation of reduced Ni particles in all catalysts. The average Ni crystallite size was calculated using the full width at half maximum (FWHM) of the (200) reflection (inset in Fig. 2a, Table S7) and the Scherrer equation [52]. In general, the average Ni crystallite size followed the ranking 15Ni/MG70 > 15Ni/MG28 ~15Ni1Pt/MG70 > 15Ni1Pt/MG28, with values ranging between 4 and 8 nm. No reflections corresponding to Pt fcc (ICSD 243678) could be identified, which excludes the presence of ordered Pt domains larger than 3–4 nm. Among the mono- and bimetallic samples, the shift in ° *2θ* of the Ni *fcc* (200) reflection did not exceed 0.05° compared to the position of the pure metallic Ni (51.85°). Moreover, no trend was observed when comparing the mono- and bimetallic samples (see Table S7 and detailed calculations in the SI). The minimal and incoherent shifts observed among the mono- and bimetallic catalysts are most likely due to peak asymmetry in the XRD measurements, *i.e.*, they fall within typical measurement/peak-broadening uncertainties. HAADF-STEM measurements combined with EDXS mapping were employed to further characterize the pre-reduced mono- and bimetallic catalysts. The results obtained are displayed in Figure S9 and Figure S10, respectively. In the case of 15Ni/MG70, a preferential spatial association of Ni with Mg, and opposed to Al species was observed in their corresponding EDXS maps, which is consistent with the observations derived for the as prepared samples (calcined state, Figure S9). On the other hand, for 15Ni/MG28, Al and Mg spatial distributions are overlapping, in line with the stochiometric Mg:Al ratio and the fact that $MgAl_2O_4$ represents the main crystalline phase in this case. For this sample, no preferential spatial association between Ni and Mg can be derived after the pre-reduction step on their EDXS maps (Figure S9). Consequently, the difference between the Ni particle size in the two monometallic catalysts is significant. As summarized in Fig. 3, average nanoparticle (NP) sizes of 11.9 ± 3.5 nm and 8.6 ± 2.1 nm were obtained for the 15Ni/MG70 and 15Ni/MG28 samples, respectively. Both Pt-promoted catalysts exhibit decreased average NP sizes; specifically, 5.9 ± 4.1 nm and 4.4 ± 2.3 nm were derived for the 15Ni1Pt/MG70 and 15Ni1Pt/MG28 samples, respectively. The relatively high standard deviation/relative error obtained for both bimetallic samples is caused by the bimodal particle size distribution, with over 30 % of the measured NPs having a size between 1 and 3 nm. At the same time, Pt appears to be more homogeneously distributed in the 15Ni1Pt/MG28 sample relative to the 15Ni1Pt/MG70 catalyst. When comparing the spatial distribution of Ni and Pt in the collected EDXS maps (Figure S10) for the bimetallic catalysts, no perfect Ni-Pt co-location could be established. To further investigate these aspects, concentration profiles of Ni (Ni-K line) and Pt (Pt-L line) within single nanoparticles were determined after the quantification of EDXS line scans. These analyses, carried out for selected nanoparticles, revealed inhomogeneities in the Ni-Pt concentrations and spatial distribution at

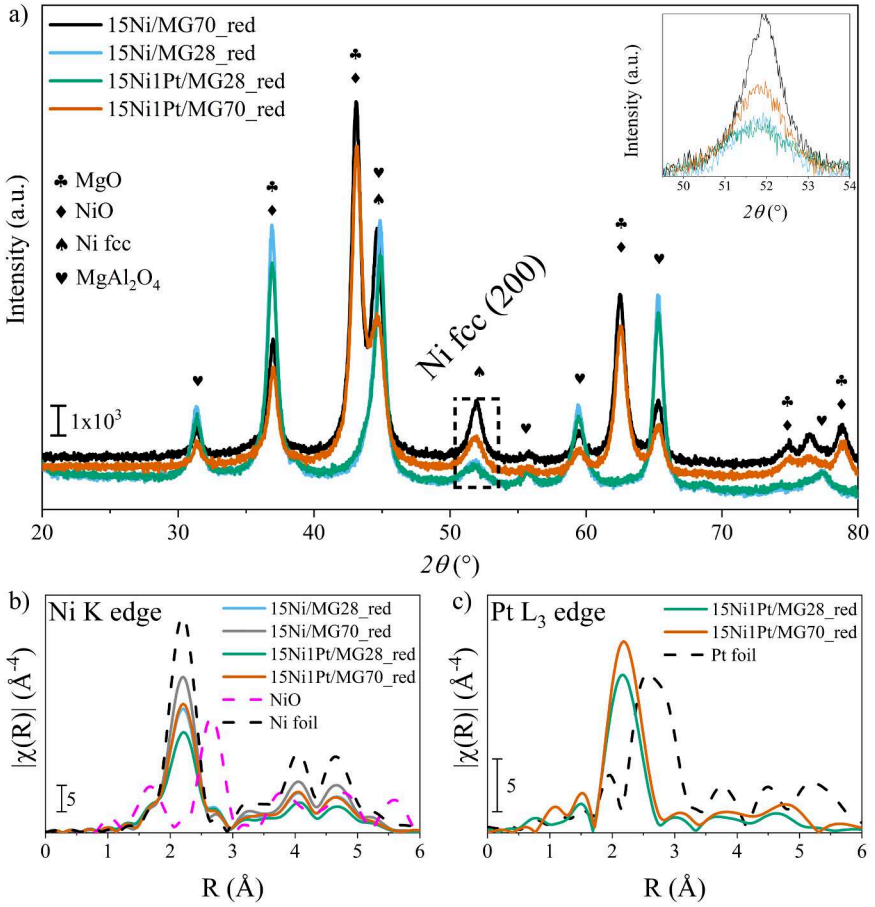

Fig. 2. (a) XRD patterns of the reduced catalysts(λ = 1.5406 Å). Inset in (a) shows the (200) reflection of Ni *fcc* appearing for all catalysts after reduction. FT-transformed EXAFS (not phase shift corrected, k^3 weighted) at (b) Ni K and (c) Pt L_3 edges for the pre-reduced catalysts, together with the corresponding references (Ni and Pt foil, NiO, dashed).

atomic level, suggesting a decrease in Pt content with increasing NP size (Figure S11 and Table S8), in particular for 15Ni1Pt/MG28. Despite the simultaneous presence of Ni and Pt in Ni-rich nanoparticles is indicated by the EDXS (Figures S10-S11) and XAS investigations (Fig. 2) for both bimetallic samples, no change in crystal structure or lattice parameters from the ones of Ni *fcc* were detected during the HRTEM evaluation of single nanoparticles (Figure S12-S13). Analogous, for Pt-rich nanoparticles a good agreement was found between the experimental two-dimensional FT and the calculated diffraction pattern of bulk *fcc* Pt. As detailed in the supporting information, in both cases this is consistent with the presence of only minor traces of the other element, which are insufficient to influence the primary lattice parameters. From previous studies, it is known that anchoring of Ni clusters on MgO is inversely proportional to the cluster size [53]. Furthermore, for bimetallic Ni-Pt nanoparticles with Ni:Pt molar ratio > 8, (as in the current study) Pt atoms are expected to be mostly located on the surface and subsurface of Ni-Pt NPs, increasing their thermal stability towards sintering [54]. Considering this information and the results of the TPR measurements (Figure S8), the bimodal size distribution observed in the pre-reduced bimetallic catalysts can be rationalized. In particular, an initial formation of Pt clusters (up to 300 °C) would be followed by the reduction of Ni species in Pt proximity *via* hydrogen spillover and formation of small Pt-rich particles (up to 700 °C). At the same time, the slow nucleation and reduction of Ni species occurs further away from Pt. The overall growth of Ni-rich particles is expected above 700 °C.

Since electron microscopy techniques only provide local information for small portions of sample, complementary *ex situ* XAS measurements were performed for the pre-reduced catalysts to obtain bulk averaged information on the catalyst structure [43]. The XANES regions collected at both Ni K and Pt L_3 edges are reported in Figure S14. Around Ni K edge, all spectra show isosbestic points which are shared with the Ni foil and NiO references. This implies that each catalyst spectrum can be described as linear combination of these two references. Linear combination fitting (LCF) was therefore performed and the results are reported in Table S9, indicating partial reoxidation of Ni particles to NiO during exposure to ambient air. When comparing the metallic Ni fraction with the average Ni crystallite size Fig. 2a, an inverse trend between these two physical measures emerges. This may be attributed to a comparable thickness of the NiO passivation layer among the pre-reduced samples.

To further characterize the local structure of the active metals, EXAFS data were also extracted for both Ni K and Pt L_3 edges, as reported in Fig. 2b-c. At Ni K edge, the backscattering contribution of the metallic Ni-Ni at R = 2.2 Å is for all catalysts lower than that observed for the Ni foil, suggesting a CN < 12 (bulk Ni *fcc* crystal). EXAFS fitting at the Ni K edge data was performed within the boundary conditions described in Table S10 and Table S11. The results of the fits are reported in Table S12 and Figure S15. The calculated metallic Ni-Ni CNs are in the range 6.2–9.4. These trends in CN among the samples align well with those derived *via* the Scherrer equation and XRD patterns, as both calculations provide selective information on the metallic part of Ni NPs. Since pronounced reoxidation was observed after exposure to ambient air, oxidic paths modelled from NiO were added to the fitting model at the Ni K edge, improving the overall quality of the fitting. The trends in the obtained CN for the oxidic paths are in line with what those derived based on LCF of the corresponding XANES regions. In particular, samples containing larger Ni NPs present a lower fraction of oxidized Ni.

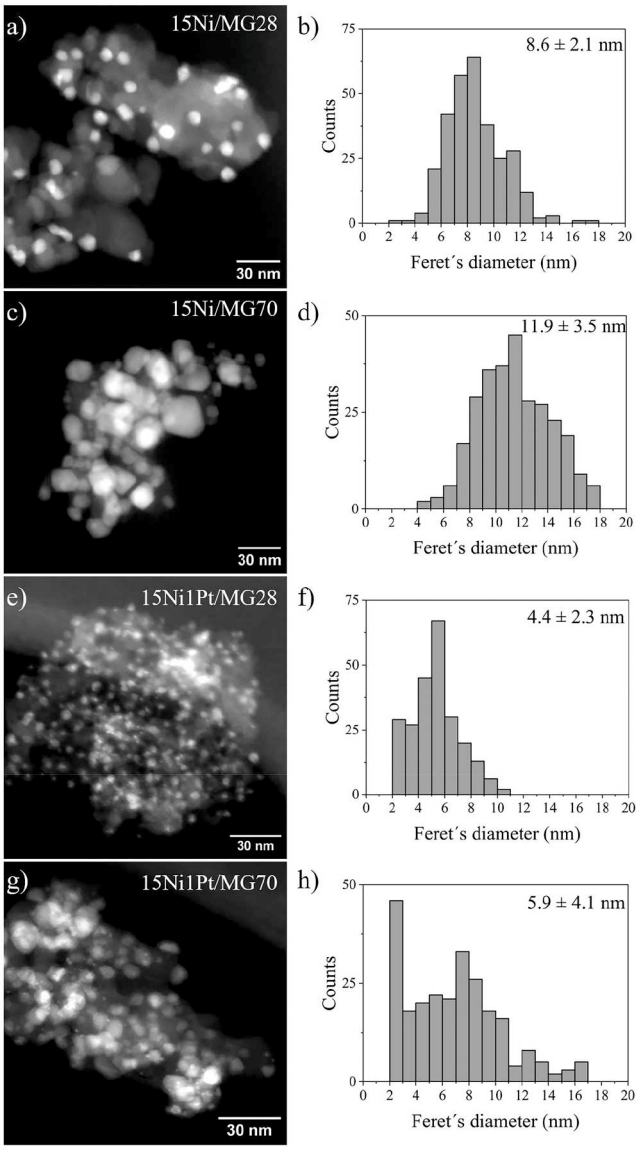

Fig. 3. HAADF-STEM images (left column) and corresponding particle size distribution* (right column) obtained for the reduced (a,b) 15Ni/MG28, (c,d) 15Ni/MG70, (e,f) 15Ni1Pt/MG28 and (g,h) 15Ni1Pt/MG70 catalysts.*300 particles counted for each sample.

Overall, the partial reoxidation of Ni NPs after exposure to air could explain the larger NP size values derived from the HAADF-STEM and EDXS data compared to those obtained from the XRD data, as the first method does not distinguish between metallic and oxidic domains. These observations emphasize the importance of using complementary characterization techniques for complex materials such as heterogeneous catalysts [55].

At Pt L_3 edge, the FT-EXAFS profiles of both pre-reduced bimetallic Ni-Pt catalysts did not reflect that of Pt metal foil, but exhibited a main scattering contribution at 2.5 Å. This difference was previously assigned to the scattering on Ni neighbors indicating formation of Ni-Pt alloyed particles [27,56]. This was further confirmed by the shoulder observed at 11575 eV in the XANES profile (Figure S14b), which was as well linked to the formation of Ni-Pt alloys [57,58]. Due to the high Ni:Pt molar ratio (approximately 40–50, see Table 1) in the bimetallic samples, the formation of alloyed particles could not be confirmed by the measurements at Ni K edge, which are dominated by scattering of other Ni atoms. The fit of the FT-EXAFS data obtained at the Pt L_3 edge confirmed the Ni-Pt interaction. A CN of 6.0 ± 1.0 and 7.9 ± 1.0 was obtained for 15Ni1Pt/MG28 and 15Ni1Pt/MG70, respectively. Details on the fitting procedure and results are reported in Table S13-S15 and Figure S16. Compared to previous findings [27], in which the *in situ* analysis of similar catalyst after reduction and without exposure to air resulted in higher (*i.e.* 9.0 ± 0.2) Ni-Pt coordination numbers, the difference in this study was attributed to passivation of the Ni nanoparticles due to the exposure to ambient air. On the other hand, the similarity between the refined CN for Ni-Pt and Ni-Ni in the two bimetallic catalysts points at random bulk alloy formation.

In summary, the analysis of the FT-EXAFS data obtained for the pre-reduced catalyst state, combined with the XRD results and HAADF STEM-EDXS characterization allowed to rank the Ni particle size as follows: 15Ni/MG70 >> >15Ni1Pt/MG70 > 15Ni/MG28 > 15Ni1Pt/MG28 (Table S16). Thus, a lower Mg:Al ratio and/or Pt addition in Ni-based catalysts promote the formation of smaller Ni NPs during the activation in H_2. In particular, the impact of the Mg:Al ratio on the average NP size could be traced back to the initial Ni-Mg interaction and distribution, which is especially promoted during the preliminary calcination step. Subsequently, the high local concentration of Ni due to the formation of $NiMgO_X$ favors the growth of larger Ni NPs on the MG70 support during catalyst reductive treatments. Furthermore, in line with previous studies on analogous materials [27], the EDXS and EXAFS characterization results confirmed the coexistence of Ni-rich, Pt-rich and pure Ni phases in the reduced bimetallic catalysts.

3.3. Catalytic activity during transient steam reforming of methane

As reported in Fig. 5, first light-off/light-out (LOff/LOut) activity tests were conducted to verify the ability of the mono- and bimetallic catalysts to activate CH_4 in the pre-reduced state, according to the procedure described in Figure S17. At the same time, their stability during two consecutive heating/cooling (light-off/light-out) cycles in RM was evaluated.

For comparison, Figure S18 shows the CH_4 conversion and CO, CO_2 yields at thermodynamic equilibrium under the applied testing conditions (pressure, feed composition), which were calculated considering the steam reforming of methane (SRM, Eq. 2) and water gas-shift (WGS, Eq. 3) as dominant reaction paths.

As expected, all the catalysts were able to activate CH_4 but strong differences in activity were noticed already during the first light-off in RM (Fig. 4). As general indicators of catalytic activity, the onset temperature (T_{onset}) and the temperature corresponding to 50 % CH_4 conversion (T_{50}) were extracted from the light-off curves and are reported in Table S17. The observed variations in catalyst performance could be rationalized considering the distinct structural characteristics and composition of the investigated systems. Additionally, the possible re-oxidation of metallic Ni to Ni^{2+}, and the formation of $NiMgO_X$ oxides under reaction conditions need to be considered at low temperatures before the reaction onset [27], when steam is present and methane is not yet converted into reducing agents (*i.e.*, H_2 and CO).

When Pt was present as a promoter, the reaction onset was between 230 and 240 °C for both bimetallic samples. In contrast, for the monometallic Ni catalysts CH_4 conversion started at higher temperatures between 420 and 440 °C. Accordingly, the following ranking was obtained for the T_{onset} values during the first LOff: 15Ni1Pt/MG28 ~ 15Ni1Pt/MG70 < < 15Ni/MG28 < 15Ni/MG70. The same trend was obtained for the T_{50} values. Further catalytic data are reported in Figure S19. The results obtained indicate that both bimetallic catalysts are able to activate methane at similar temperatures, while the monometallic Ni-based samples showed increasing reaction onset temperatures with increasing the Mg:Al ratio: 417 °C and 441 °C for 15Ni/MG28 and 15Ni/MG70, respectively. This tendency is most probably caused by the strong interaction between Ni species and excess MgO, which leads to an enhanced diffusion of the oxidized Ni^{2+} ions into the MG70 support before the reaction onset [27].

To verify the stability of the catalysts under dynamic conditions, a

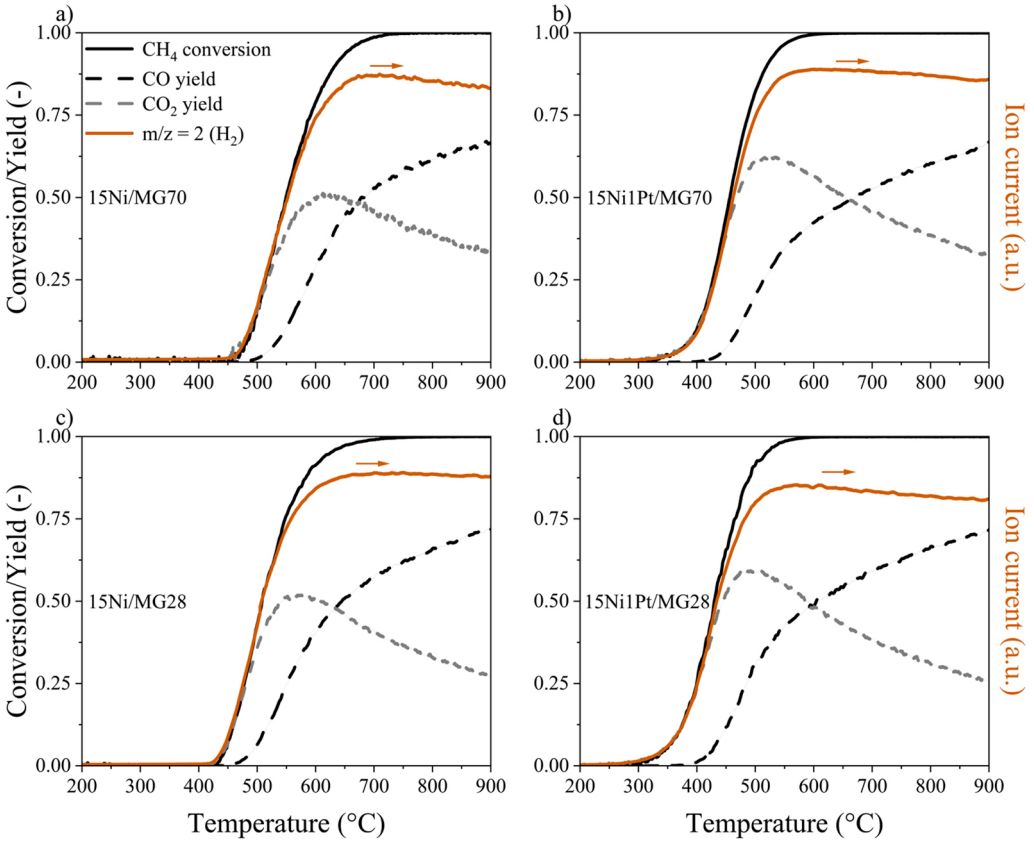

Fig. 4. Catalytic activity during light-off (LOff) in reaction mixture (RM, 0.66 vol% CH_4, 2 vol% H_2O, N_2 balance) after pre-reduction. a) 15Ni/MG70, b) 15Ni1Pt/MG70, c) 15Ni/ MG28, d) 15NiPt/ MG28.

second consecutive heating/cooling cycle in RM (red curves in Fig. 5) was performed. Additional data are provided in Figure S20. Only the bimetallic Ni-Pt catalysts maintained a low T_{50} over the two consecutive cycles (between 430 and 460 °C). When comparing the ΔT_{onset} and ΔT_{50} of the bimetallic catalysts (Table S17), no significant difference was observed between them. Independent of the support composition, this behaviour indicates similar active species for methane activation in both samples. Conversely, the difference between the T_{50} values (ΔT_{50}) measured during the first and second light-off curves for the two monometallic Ni-based catalysts is larger than 100 °C. In particular, the effect of the support composition is clear for the 15Ni/MG70 sample, with a ΔT_{50} of 250 °C whereas this difference is only 114 °C for 15Ni/ MG28. This behavior aligns with the higher stability under dynamic reaction conditions of the MG28 supported catalyst, which contains a lower Mg:Al ratio.

In the next step, the ability of the as prepared catalysts (calcined at 500 °C) to undergo autoactivation under reaction conditions was evaluated. For industrial applications, this attribute is highly valuable, as it allows avoiding the use of an additional H_2 stream for catalyst reductive activation since such conditions are always demanding and pose safety issues for the operation of the reactor. The results obtained indicate that only the bimetallic samples are able to activate CH_4 without a pre-reduction step (Figure S21 and Figure S22). The reaction onset temperature was 277 °C and 305 °C for 15Ni1Pt/MG28 and 15Ni1Pt/MG70, respectively. As no Ni-Pt interaction was revealed in the as prepared catalyst state during catalyst characterization, the observed activity for the bimetallic catalysts is likely due to methane activation over Pt. The similar reaction onset temperatures measured for the bimetallic samples in the as prepared and pre-reduced state (Table S18 and Table S17, respectively) further corroborate this hypothesis. Nevertheless, although both Ni-Pt bimetallic catalysts exhibited similar reaction onset temperatures during autoactivation, their conversion profiles are significantly different. In fact, it was recently shown [27] that once Pt starts to activate CH_4 and H_2 is produced, the oxidized Ni in the bimetallic catalysts is reduced as well. This process further increases the number of active sites for SRM. Consequently, the 15Ni1Pt/MG28 catalyst converts 50 % of methane at 460 °C, while this conversion is achieved over 15Ni1Pt/MG70 only at 550 °C. This difference could originate in the distinct reducibility of Ni species in the two catalysts (Figure S8). This hypothesis is confirmed by the ability of the corresponding 15Ni/MG28 monometallic sample to autoactivate, despite the reaction onset for CH_4 conversion is only around 750 °C. On the other hand, the 15Ni/MG70 sample, which contains significant amounts of $NiMgO_X$ species, did not show any notable conversion during the light-off, and only a slight increase of the H_2 MS signal was detected above 800 °C.

Overall, these preliminary tests show that a lower Mg:Al ratio and/or Pt addition are effective ways to diminish or even prevent catalyst deactivation under dynamic conditions, and also promote catalyst autoactivation in the SRM reaction mixture. Moreover, Pt seems to contribute rather independently to the catalytic reaction, as also reported by previous investigations on similar materials [27].

3.4. Catalytic activity after simulated reactor shut-down in different gas atmospheres

In the next step, a systematic investigation of catalyst deactivation under different gas atmospheres was carried out following the procedure described in the experimental section and in Figure S23. Briefly, a catalyst conditioning protocol was initially applied to standardize its initial state throughout the extensive testing campaign. This consisted of an activation step in 5 vol% H_2 up to 900 °C, followed by holding the

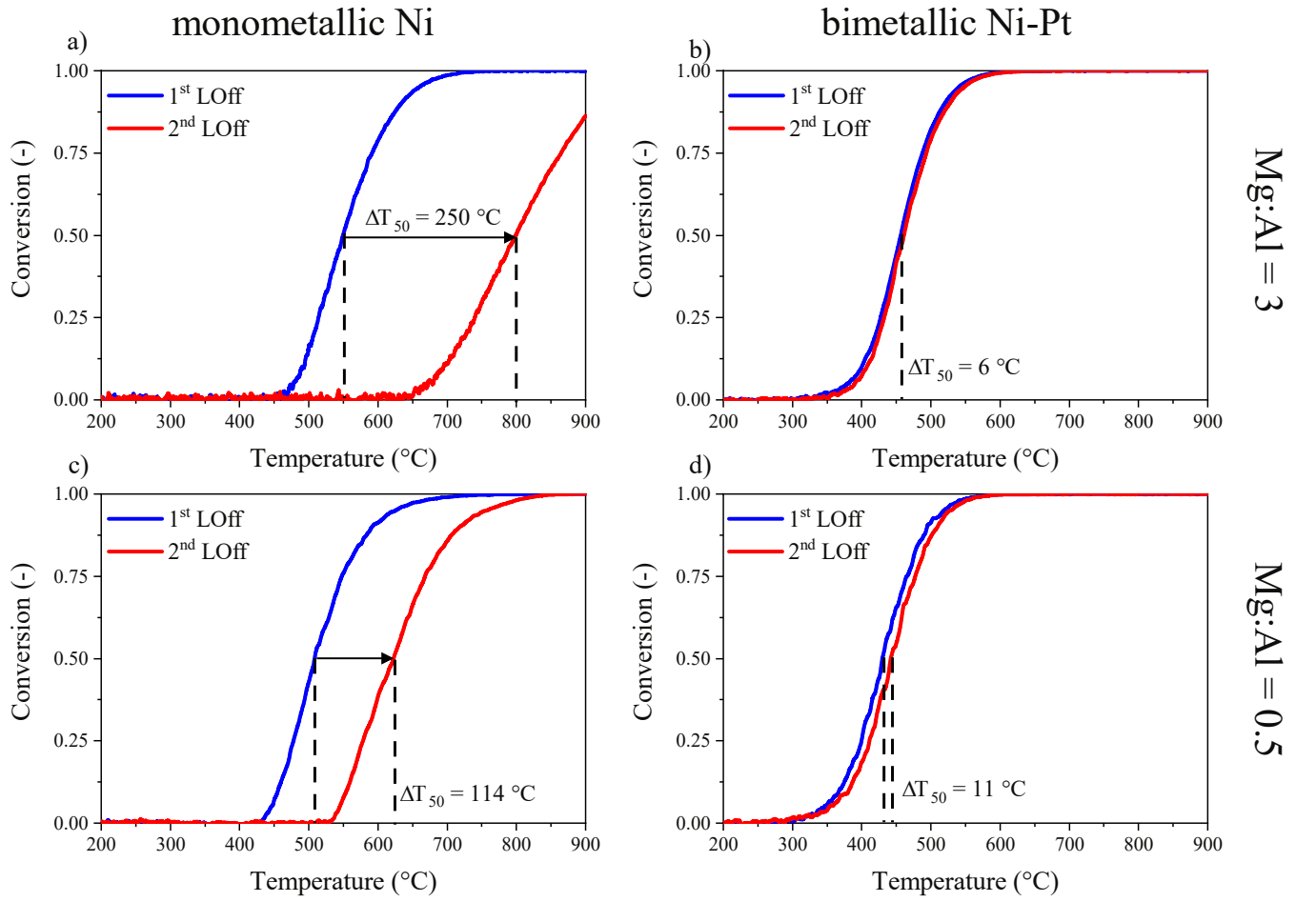

Fig. 5. CH_4 conversion during two consecutive light-offs (LOff) in reaction mixture (RM, 0.66 vol% CH_4, 2 vol% H_2O, N_2 balance) after pre-reduction. a) 15Ni/MG70, b) 15Ni1Pt/MG70, c) 15Ni/MG28, d) 15NiPt/MG28.

catalyst under RM at full methane conversion for 2 h at the same temperature. To simulate the reactor shut-down, the catalyst was exposed afterwards to various gas mixtures (RM, inert or vapor-saturated inert) during reactor cooling from 900 °C to RT. Finally, a heating/cooling ramp in RM was performed to evaluate the residual catalytic activity.

For all these experiments, *ex situ* pre-reduced samples were used. During step (i), the partially oxidized Ni species (Figure S14) were fully reduced, as indicated by the *in situ* XANES spectra reported in Fig. 6. The formation of Ni NPs was confirmed by complementary *in situ* XRD data collected at $\lambda = 1.5120$ Å (Figure S24), which show the characteristic Ni *fcc* (200) diffraction peak (around 51° *2θ*) with increasing reduction temperature for all catalysts. Regarding the final crystallite size, the broadening of the metallic Ni peak at 900 °C followed the trend 15Ni/MG70 < 15Ni1Pt/MG70 ~ 15Ni/MG28 < 15Ni1Pt/MG28. This is inversely proportional to the crystallite size and in line with data obtained from the *ex situ* characterization of the pre-reduced catalysts (Fig. 3).

During the step (ii), all catalysts were subjected to high temperature (900 °C) and reducing conditions, as complete CH_4 conversion led to H_2 and CO formation. For the duration of this step, CH_4 conversion and CO and CO_2 yields remained stable (Figure S25) over all samples, in agreement with the thermodynamic equilibrium. As indicated by the *in situ* XAS and XRD data respectively in Fig. 6 and Figure S26, Ni remained in reduced state, with no further increase in Ni crystallite size.

Generally, the deactivation induced by the simulated shut-downs is expected to impact the catalytic activity recorded in the subsequent light-off, performed up to 900 °C. Accordingly, the greater the deactivation extent, the higher the reaction onset temperature and T_{50} expected during the latter step. In case of severe deactivation, no methane conversion is anticipated.

In comparison to the activity of the *in situ* pre-reduced catalysts (blue lines in Fig. 5), cooling in RM only led to an increase of T_{onset} for all investigated samples (Fig. 7a, Table S19). In particular, during the subsequent light-off in RM, a ΔT_{onset} of over 100 °C was noticed for the monometallic samples, while only an increase of less than 35 °C was encountered for the bimetallic samples (Table S19). As found out in a recent study [27], the presence of Pt hinders the oxidation of Ni during the reaction light-out and maintains higher catalytic activity in bimetallic samples. However, after this "controlled" shut-down procedure, all mono- and bimetallic samples were still able to convert methane and achieve full conversion during the light-off to 900 °C (Fig. 7a and Figure S27). Over the Ni-Pt bimetallic catalysts, methane is converted above 275 °C, and just minor differences were noticed between the MG28- and MG70-supported catalysts. As described in the Section 3.3, for bimetallic samples Pt promotion of methane activation is expected at low temperatures when Ni is partially oxidized [27]. On the other hand, monometallic Ni catalysts convert a significant amount of methane only above 550 °C. Additionally, despite the monometallic catalysts have a similar onset temperature, a difference in T_{50} values of ~25 °C was noticed, with a higher T_{50} measured for 15Ni/MG28. This difference could be ascribed to the dynamic interaction between Ni species and MgO, which is especially promoted during the last part of the cooling ramp in reaction mixture when CH_4 is not converted anymore and water vapors are still present. Under these circumstances, partial oxidation of Ni particles to NiO and incorporation of Ni^{2+} ions into $NiMgO_X$ is expected [27]. Hence, an increased interfacial area between oxidized NPs

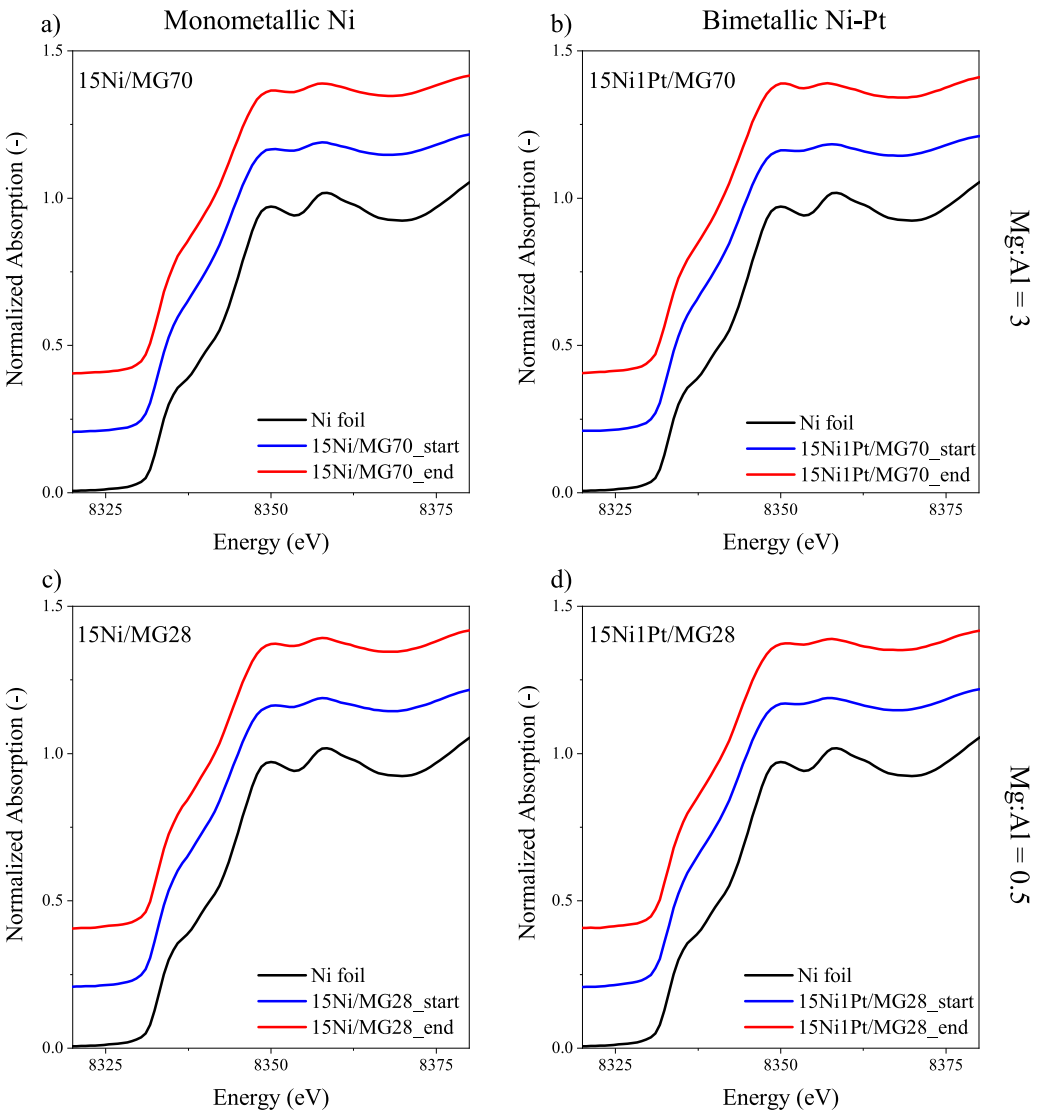

Fig. 6. *Operando* XANES spectra (offset) recorded at Ni K edge during the holding time at 900 °C. Comparison is done between the Ni foil (black curves), the spectra at the end of the TPR in 5 vol% H_2/He (red curves) and the spectra at the end of the 2 h holding time in RM (blue curves).

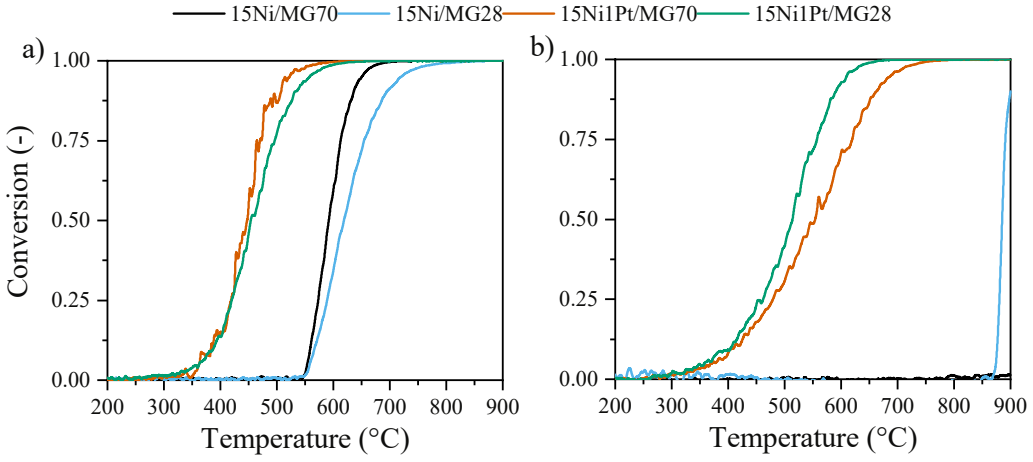

Fig. 7. CH_4 conversion during heating up in reaction mixture (RM, 0.66 vol% CH_4, 2 vol% H_2O, N_2 balance) after cooling down the reactor from 900 °C under different atmospheres. a) cooled down in RM, b) cooled down in 2 vol% H_2O/N_2.

and superficial MgO (in case of 15Ni/MG28) might increase the amount of Ni^{2+} ions migrating in the outermost layer and subsurface of mixed oxides. In conjunction with methane conversion, the resulting state is only reversed by reduction between 550 and 750 °C, as described in Section 3.1. On the other hand, the slightly larger particles that are present in 15Ni/MG70 (Section 3.2) are less prone to bulk oxidation in the reaction mixture and also expected to reduce earlier becoming active at lower temperatures.

The deactivation induced by the simulated shut-down in vapor-saturated inert atmosphere appears for all catalysts significantly more severe than that produced by cooling down the catalyst bed in the SRM gas mixture. Based on the results displayed in Fig. 7b, the monometallic catalysts are more sensitive to water presence compared to the bimetallic Ni-Pt counterparts. In particular, the 15Ni/MG70 sample did not show any CH_4 conversion during the following SRM LOff. On the other hand, the 15Ni/MG28 catalyst was still able to activate CH_4 after deactivation in water vapor, although the reaction onset occurred only at 750 °C. At the same time, both bimetallic catalysts were able to convert CH_4 already around 270 °C. A higher T_{50} value of 554 °C was measured for 15Ni1Pt/MG70 in comparison to 514 °C as recorded for 15Ni1Pt/MG28. The former sample also showed a less steep conversion profile and reached full conversion at higher temperatures compared to 15Ni1Pt/MG28. This behavior indicates a higher sensitivity of MG70-based catalysts towards water presence, as also revealed by the investigations reported in Fig. 5. In fact, when cooling the catalyst bed in steam (Fig. 7b) the catalysts are exposed to an oxidizing environment at higher temperatures and for a longer duration in comparison to the simulated shut-down in RM (Fig. 7a). Hence, a higher degree of Ni oxidation and even Ni NPs redispersion are expected, along with the incorporation of Ni^{2+} ions into $NiMgO_X$ and their migration in the bulk phase. The latter phenomenon is less probable in the case of MG28-supported catalysts due to the lower amount of MgO present, which explains the higher catalytic activity observed. Since a strong loss in catalytic activity was observed after the simulated shut-down in vapor-saturated inert atmosphere, Raman spectroscopy was performed on the spent samples to investigate the possible carbon formation during the following LOff/LOut (Figure S28). For a better comparison, reference Raman spectra were also measured for the catalysts in their calcined and reduced state. In general, Raman spectra of carbonaceous materials show two intense and distinct bands around 1350 cm^{-1} and 1580 cm^{-1}, namely the D and G bands [59]. In the spectra obtained for the spent catalysts, depicted in Figure S28c, the observed Raman bands are shifted with more than 30 cm^{-1} from the D band and more than 100 cm^{-1} from the G band. Since these Raman bands at ca. 1315 cm^{-1} and 1460 cm^{-1} were observed already in the calcined and reduced catalysts (Figure S28a,b), they cannot be attributed to carbon deposition under reaction conditions but rather to oxidic species already present in the catalysts before the exposure to methane steam reforming conditions.

In another experiment, the shut-down was simulated by cooling the reactor from 900 °C to RT in inert atmosphere (N_2). The conversion of methane during the subsequent light-off is shown in Fig. 8a. Similarly to the previous experiments (Fig. 7), both bimetallic Ni-Pt catalysts still activate methane below 300 °C (Table S20), while the onset temperatures for the monometallic catalysts remain above 600 °C. Furthermore, the catalysts supported on MG70 suffered more severe deactivation compared to their counterparts supported on MG28. This highlights once again the effect of the Mg:Al ratio and the resulting excess of MgO in catalyst composition on the deactivation extent. Hence, the monometallic 15Ni/MG28 catalyst fully recovered its catalytic activity after 5 min at 900 °C, in reaction mixture, as shown by the light-out conversion profile depicted in Figure S29c. On the other hand, 15Ni/MG70 did not show appreciable conversion during the subsequent light-off and light-out. The observed deactivation for this sample is comparable to that reported in Fig. 7b. This tendency is caused by the short exposure (ca. 5 min, Figure S30) to water vapors during the switch between the RM and inert gas streams at 900 °C. Due to the very high temperature, the oxidation of Ni species is expected to be very rapid, and is further amplified by the MgO presence. In contrast, for the 15Ni/MG28 catalyst containing less Mg, the short duration of exposure to water vapors during this testing procedure in comparison to the approximately 1.5 h exposure during the simulated shut-down in vapor-saturated inert atmosphere helps to rationalize the remaining activity.

To confirm the observed effect of the MgO concentration on the catalyst stability, long-term operation was simulated by conducting several start-up/shut-down cycles during 4 consecutive days. The results, depicted in Figure S31 and Figure S32, show that the monometallic catalyst supported on MG28 can sustain dynamic operation for multiple cycles. In line with the tests reported in Fig. 8a, the catalytic activity for methane steam reforming during both start-up and continuous operation at high temperatures was maintained, highlighting the beneficial effect of using a support with lower MgO content that prevents excessive incorporation of Ni species. The catalyst showed comparable T_{onset} (751 ± 4 °C), T_{50} (769 ± 8 °C) and T_{90} (794 ± 11 °C) values over the 3 start-ups (Table S21), which indicates that the catalyst did not deactivate within the boundaries of these experiments. The presence of carbon deposits on the spent sample was excluded also in this case after longer reaction time (Figure S28d).

Based on the observed trends in catalyst deactivation as a function of the gas atmosphere used during reactor cooling step, an adjusted shut-down procedure was implemented. The aim was to maintain most of

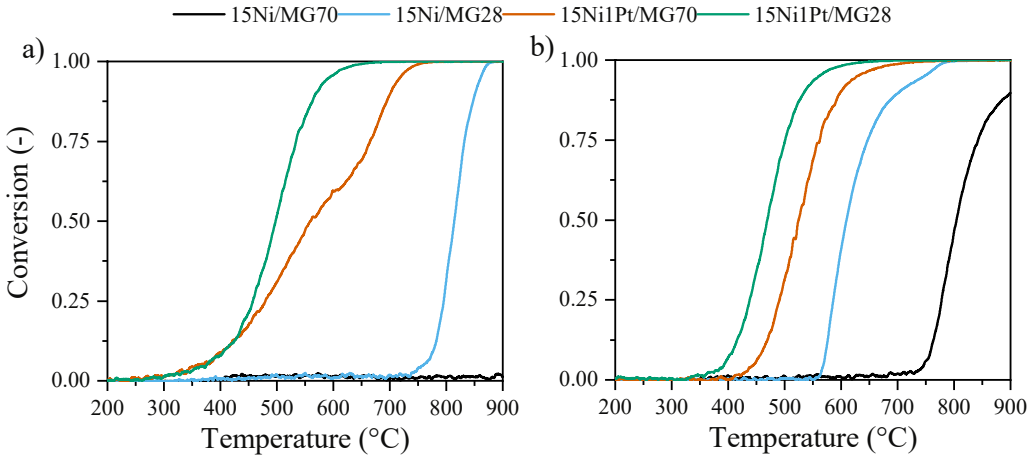

Fig. 8. CH_4 conversion during heating up in reaction mixture (RM, 0.66 vol% CH_4, 2 vol% H_2O, N_2 balance) after cooling down the reactor from 900 °C under different atmospheres. a) Cooled down in N_2, b) cooled down initially in RM, then from 600 °C in N_2.

the catalyst bed under reducing gas atmosphere and limit the exposure to H_2O vapors at high temperatures. Hence, after cooling down in RM from 900 °C to 600 °C (>95 % CH_4 conversion over all pre-reduced catalysts, red curves in Figure S19), the reactor inlet gas mixture was switched to N_2 for the rest of the cooling ramp until RT was reached. In this way, the catalysts were only exposed for a short time frame (ca. 5 min) to water vapors at 600 °C during the system purging phase. The SRM activity measured during the subsequent light-offs is reported in Fig. 8b, and can be directly compared with the CH_4 conversion obtained after reactor cooling in inert atmosphere (Fig. 8a). It can be immediately noticed that this adjusted shut-down procedure resulted in a smaller extent of deactivation for all catalysts. Both monometallic catalysts exhibited a T_{onset} for the SRM reaction at temperatures under 600 °C, and all catalysts showed lower T_{50} values in comparison to those measured during the N_2 shut-down procedure (Table S20). Nevertheless, the catalytic activity is still negatively affected compared to the SRM performance measured for the reference pre-reduced state of all Ni-based catalysts (blue curves in Fig. 5). For instance, for the pre-reduced 15Ni1Pt/MG28 catalyst 50 % conversion was achieved at 431 °C while only 20 % was reached after the adjusted shut-down procedure. All the other samples exhibited an even more pronounced drop in catalytic activity. Hence, the deactivation caused by water vapors could not be completely avoided with this reactor shut-down procedure. Interestingly, the thus obtained trend in T_{50} and T_{onset} was the same as for the switch in inert at 900 °C, *i.e.,* 15Ni/MG70 > 15Ni/MG28 > 15Ni1Pt/MG70 > 15Ni1Pt/MG28. Complementary catalytic data are additionally reported in Figure S33 and an overview of T_{onset}, T_{50} and T_{90} is provided in Fig. 9. Overall, these obtained findings further substantiate the following conclusions: (i) trace amounts of water contribute to catalyst deactivation and the deactivation extent scales with increasing exposure temperature, (ii) Pt presence in the catalyst composition and/or a lower Mg:Al ratio in the carrier material represent efficient strategies to mitigate deactivation by water vapors during reactor shut-down, (iii) the use of Pt-promoted bimetallic catalysts is necessary to retain the catalytic activity in case of prolonged exposure to water vapors at high temperatures without the need for additional reduction steps before resuming operation. To confirm and better understand these observations, extensive catalyst characterization by *in situ/operando* methods was conducted as reported in the following section.

3.5. Insights into Ni and Pt behavior by in situ/operando XAS and XRD

Systematic *in situ/operando* XAS and XRD measurements were conducted for all mono- and bimetallic samples during simulated reactor shut-down. Among the different conditions applied during the extensive testing campaign, the cooling down in H_2O/N_2 procedure was selected as the most severe model condition to examine the influence of the catalyst composition on the catalyst deactivation extent by water vapors. This condition was realized by interrupting the methane supply in RM (0.66 vol% CH_4, 2 vol% H_2O, rest inert) at 900 °C and subsequently starting the cooling of the catalyst bed to RT in $2H_2O/N_2$.

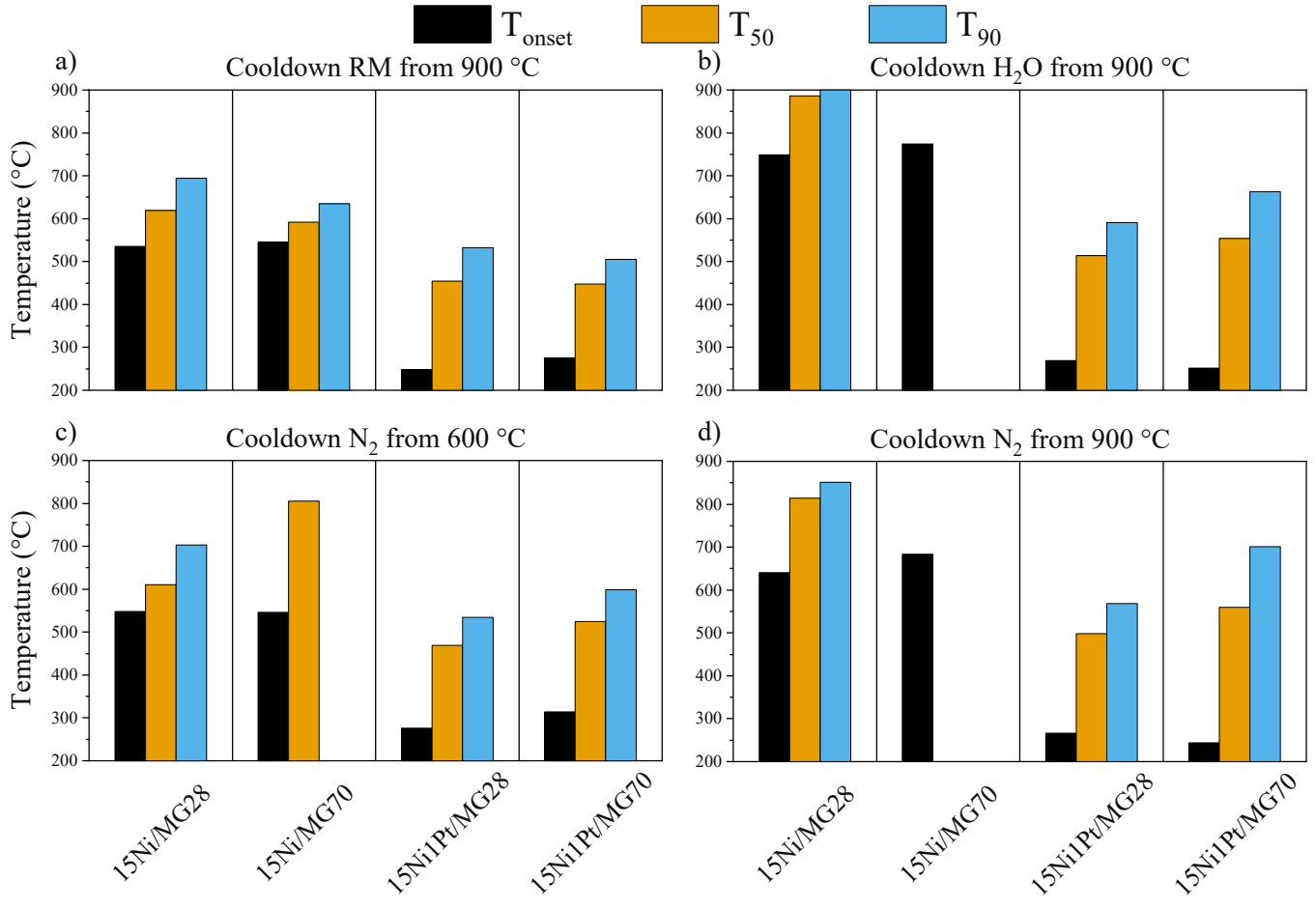

Fig. 9. Overview of onset temperatures (black), T_{50} (orange) and T_{90} (blue) for the 4 investigated catalysts during steam reforming of methane light-off carried out after different pre-treatments. (a) after cooling down in RM, (b) after cooling down in water-saturated inert from 900 °C (c) after cooling down in RM to 600 °C and from 600 °C to RT in inert, (d) after cooling down in inert from 900 °C. Please note that 90 % and 50 % methane conversion were not reached before reaching 900 °C when only 1 or 2 bars, respectively, are shown.

A first insight into the nature of Ni species generated during the simulated shut-down in water-saturated inert was obtained from the results of the linear combination fitting of the Ni K edge XANES region (Figure S35a). Since the metallic Ni and NiO components were not sufficient to reconstruct the spectra of the deactivated samples, the contribution of the $NiMgO_X$ reference was considered. This is based on our previous investigations, which showed that other phenomena rather than solely Ni oxidation to NiO occur during the simulated shut-down protocol [27]. More precisely, during exposure of MG70-based mono- and bimetallic Ni-Pt samples to the SRM gas mixture under transient heating/cooling cycles Ni oxidation and incorporation in $NiMgO_X$ oxides was observed at low temperatures and low methane conversion. Accordingly, Fig. 10 shows the LCF results for the *in situ* Ni K edge XANES spectra collected during cooling down the catalyst bed in H_2O/N_2. In general, progressive oxidation of Ni species was observed in all investigated samples, and especially in the monometallic ones. The onset of the oxidation process corresponds to the switch of the gas atmosphere from RM to H_2O/N_2 at 900 °C. In comparison with the study by Tusini *et al.* [27], in the present work the catalysts were exposed to water vapor in the absence of reducing agent for longer time and from higher temperatures, with the aim of emphasizing Ni oxidation and highlighting catalytic and structural differences arising from different catalyst compositions. Hence, for the 15Ni/MG70 catalyst a strong and continuous oxidation was observed throughout the entire cooling ramp, leading to a final composition of 8 ± 4 % Ni, 57 ± 7 % NiO, and 35 ± 8 % $NiMgO_X$.

On the other hand, for the 15Ni/MG28, 15Ni1Pt/MG70, and 15Ni1Pt/MG28 samples three regions could be distinguished in the evolution of the different reference components: a high temperature region (~900–820 °C) where very fast oxidation of Ni species was observed, an induction period with a slower oxidation rate, and a low temperature region where further oxidation of metallic Ni occurs at an intermediate reaction rate. In contrast, for the 15Ni/MG70 catalyst, the first region was broader (900–750 °C) and was followed by a temperature interval where Ni species were oxidized at an even higher rate. In the first region, NiO was formed in all catalysts accompanied by $NiMgO_X$ in the case of the MG70 supported catalysts. However, the oxidation extent within this high temperature range is increased for Ni species in both bimetallic samples, reaching 52 % and 23 % in case of 15Ni1Pt/MG70 and 15Ni1Pt/MG28, respectively. In comparison, in the monometallic samples, only 19 % and 17 % of the Ni species are oxidized at 820 °C in the case of 15Ni/MG70 and 15Ni/MG28, respectively. According to previous literature, Pt addition stabilizes Ni against oxidation. Nevertheless, the presence of smaller Ni particles in the bimetallic samples (30 % in the 1–3 nm size range) might explain this behavior, given their increased sensitivity towards Ni reoxidation [60,61].

During the following intermediate temperature range, the diffusion of Ni^{2+} ions into MgO lattice to form $NiMgO_X$ becomes dominant for the MG70 supported samples and is also noticeable for the MG28 catalysts. The lower rate of NiO formation in 15Ni/MG28, 15Ni1Pt/MG70, and 15Ni1Pt/MG28 between ~820–550 °C might be related to the intrinsic properties and the interaction of Ni NPs with the carrier material.

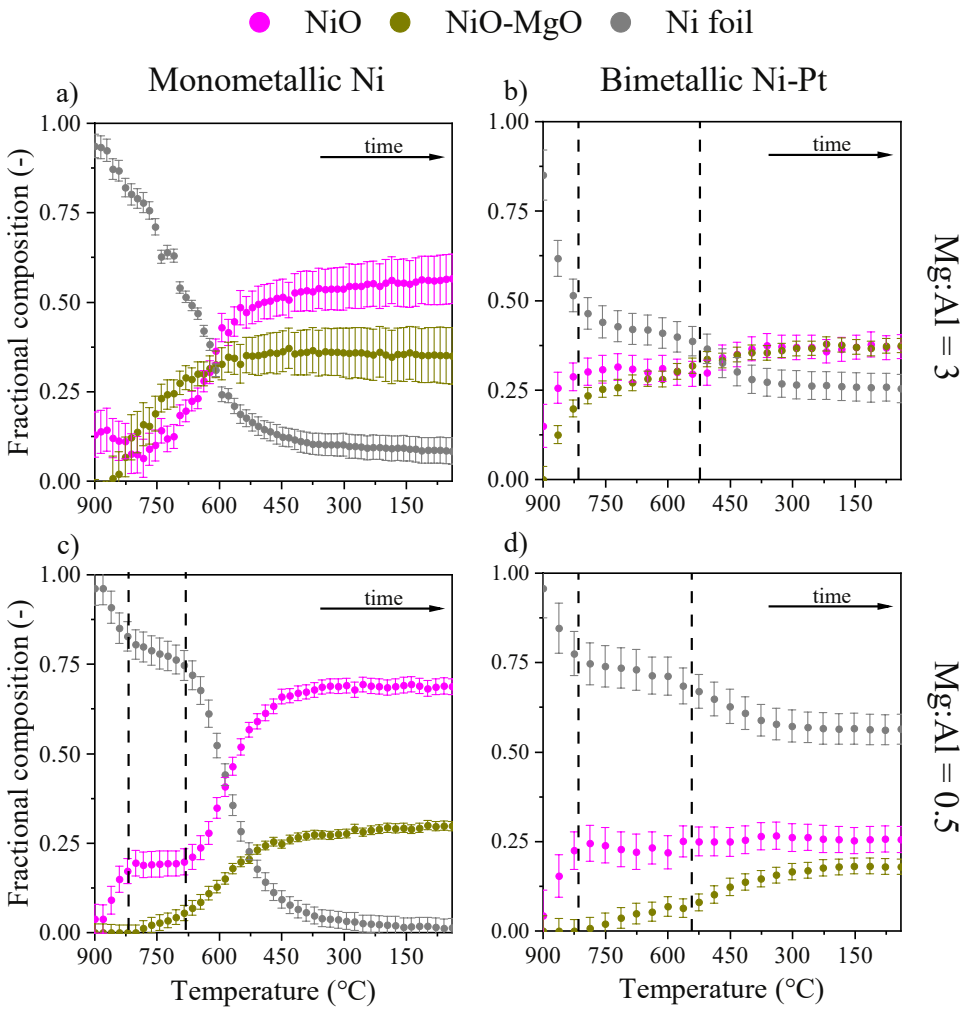

Fig. 10. Results from LCF of *in situ* XANES at Ni K edge during cooling down in H_2O-saturated inert from 900 °C to RT for (a) 15Ni/MG70, (b) 15Ni1Pt/MG70, (c) 15Ni/MG28 and (d) 15Ni1Pt/MG28. Pt L_3 edge data for the two bimetallic catalysts show that Pt remains in reduced state during the same procedure.

Alternatively, methane traces that are still present in the system might play a role in stabilizing reduced Ni during this stage. However, as all catalysts were treated in a similar manner, the different oxidation trends and generated species are most probably the result of the interplay between particle size, metal-support interaction and Pt promotion. In particular, under the transient reaction conditions of this experiment, the oxidation of large Ni particles is expected to advance slowly and to be assisted by $NiMgO_X$ formation, likely at the interface with the catalyst support (Fig. 10a,c). As this process progresses and the size of Ni particles decreases, the oxidation rate apparently increases as the temperature drops. In fact, the formation of NiO-like species in our study followed closely the formation of $NiMgO_X$ even at lower temperatures. At the end of the cooling ramp the molar ratio between NiO and $NiMgO_X$ is 2.3 and 1.6 for 15Ni/MG28 and 15Ni/MG70, respectively, indicating that a lower Mg:Al ratio hinders the incorporation of Ni^{2+} ions in the MgO matrix. On the other hand, the metallic Ni contribution is below 10 % in both cases, indicating severe oxidation of Ni species. Additionally, the FT-EXAFS profiles of 15Ni/MG28 and of 15Ni/MG70 (Figure S35c and Figure S36) resemble the ones of the NiO or $NiMgO_X$ references, respectively.

For the bimetallic catalysts, substantially higher metallic Ni fractions of 56 ± 4 % and 25 ± 4 % were maintained in the case of 15Ni1Pt/MG28 and 15Ni1Pt/MG70, respectively. These two values differ significantly despite both bimetallic catalysts having similar Ni:Pt ratios (Table 1). Nonetheless, a similar molar ratio close to 1 between NiO and $NiMgO_X$ was obtained at the end of the cooling ramp for both samples. The trends derived from the LCF of the XANES region were supported by the FT-EXAFS data obtained at Ni K edge for the deactivated catalysts, as reported in Figure S35c and Figure S36. Compared to the monometallic samples, the formation of both NiO and $NiMgO_X$ seems to be hindered by the presence of Pt, which additionally constrains the redox response of Ni species. This tendency is probably due to its noble metal character that is shared with Ni in the alloyed particles. In this regard, Moraweck *et al.* suggested a partial charge transfer between Ni and Pt based on spectroscopic and theoretical investigations [57]. Particularly for the MG28-based bimetallic catalyst, the effect of the lower MgO concentration combined with the noble metal addition resulted in the lowest oxidation extent of Ni particles during cooling down in vapor saturated inert atmosphere despite this sample containing the smallest Ni particles. The influence of Pt on the Ni state was confirmed also by the *in situ* XAS measurements at Pt L_3 edge. After the cooling ramp in the 2 vol% H_2O/N_2 atmosphere, similar profiles were obtained for the *in situ* XANES spectra measured at the end of the shut-down step to those collected for the pre-reduced bimetallic catalysts (Figure S35d vs. Figure S14b), suggesting the retention of the Ni-Pt interaction even after cooling down in H_2O/N_2.

The corresponding *in situ* XRD data collected during the cooling down in H_2O/N_2 (Fig. 11) confirmed the rather early (above ~750 °C, within 15 min from the switch) disappearance of the Ni *fcc* (200) reflection for all catalysts. This behavior indicates a progressive decrease in particle size and loss of ordered metallic Ni domains. In particular, the reflection around 51° *2θ* is visible in all catalysts after the interruption of the methane supply. While for the Ni-Pt bimetallic catalysts it is noticeable only during the first scan at 900 °C, for the monometallic

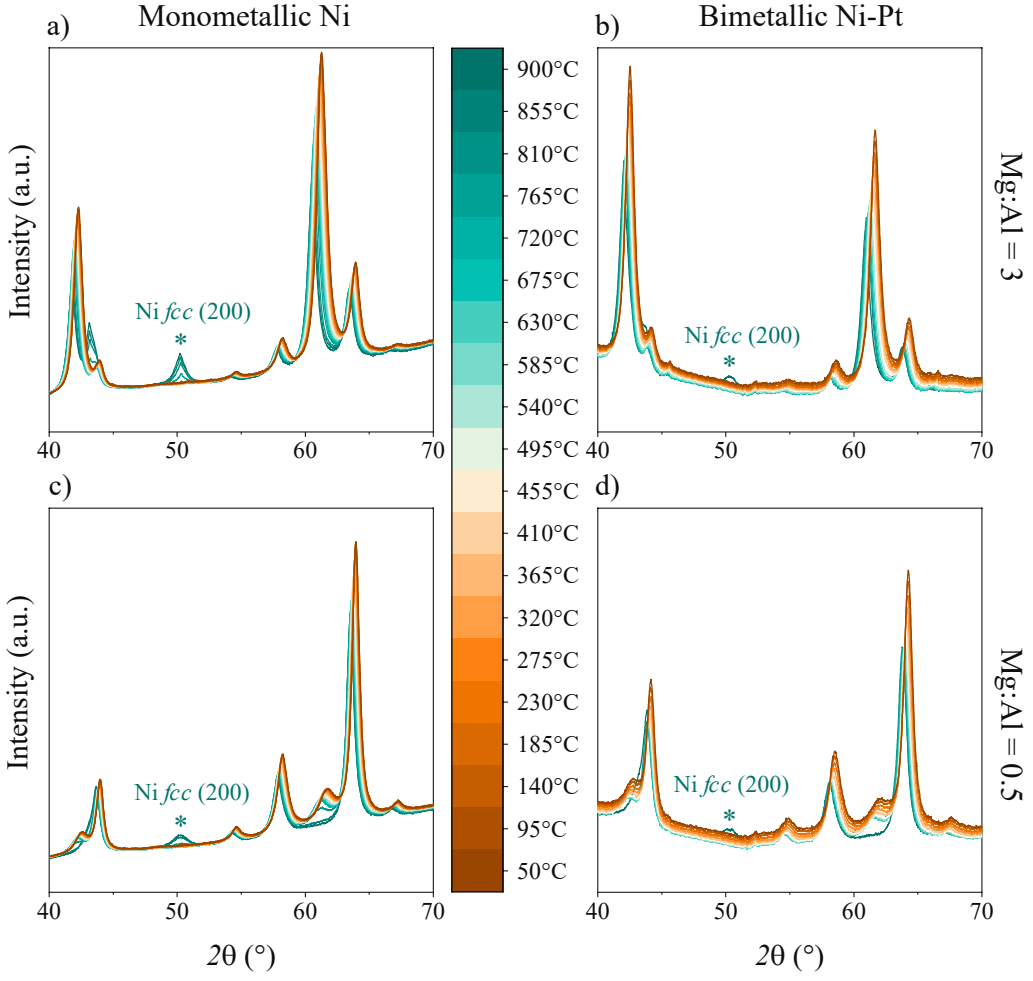

Fig. 11. Synchrotron XRD patterns (λ = 1.5120 Å, 2θ region 40–70°) measured during *in situ* cooling down in H_2O-saturated inert. (a) 15Ni/MG70, (b) 15Ni1Pt/MG70, (c) 15Ni/MG28, (d) 15Ni1Pt/MG28.

catalysts this XRD pattern disappears only below ~750 °C after several minutes in H_2O/He at high temperatures. These variations in the XRD patterns align to the change in the oxidation rate of Ni species before the induction phase, as derived based on the *in situ* XAS measurements (Fig. 10). This trend could be explained by the presence in the monometallic catalysts of larger Ni NPs (mostly up to 20 nm, see Fig. 3a,c), which are more resistant to oxidation [60,61]. Additionally, for the two catalysts supported on MG28, the conversion of metallic Ni into NiO and $NiMgO_X$ is easily discernible around 62° *2θ,* in agreement with the XAS results.

Overall, the combination of *in situ* XAS and XRD investigations on the catalyst state during simulated reactor shut-down in 2 vol% H_2O/N_2 provided a deeper understanding of the catalyst sensitivity towards oxidation due to water presence for both monometallic Ni and bimetallic Ni-Pt catalysts supported on Mg-Al mixed oxides. In the case of the bimetallic catalysts, the combined XAS and XRD results suggest the formation of small (below the XRD detection limit) and alloyed Ni NPs, whereas for the monometallic catalysts the results indicate almost complete transformation into NiO and $NiMgO_X$.

3.6. Impact of the different reactor shut-down protocols on the catalyst structure

Considering its higher sensitivity to oxidation, the spent 15Ni/MG70 sample was chosen to investigate the impact of the different catalyst deactivation protocols on the catalyst structure. For this purpose, *ex situ* XAS spectra were collected at Ni K edge at the end of the different testing procedures reported in Section 3.4 (cooling in controlled atmosphere followed by a light-off/light-out SRM cycle). The obtained EXAFS data are shown in Figure S34a. By visual comparison of the different EXAFS profiles, a similar state of Ni can be identified in the spent 15Ni/MG70 sample after the procedure involving the reactor shut-down in N_2 saturated with water vapor as that measured for the freshly prepared sample (calcination at 500 °C in static air). As described in Section 3.1, in the as prepared catalyst most of the Ni species are strongly interacting with the support material leading to the formation of $NiMgO_X$ mixed oxides [27]. The corresponding LCF results (Figure S34b) confirmed this hypothesis, with $NiMgO_X$ species accounting for more than 80 % in the two mentioned cases, along minimal presence of NiO.

After the modified shut-down procedure, which minimized the time and temperature range of exposure to water vapor (SRM gas mixture to 600 °C followed by N_2 until RT), the obtained EXAFS spectrum resembles that of the as prepared 15Ni/MgO reference but also encompasses characteristic EXAFS oscillations of metallic Ni around 5.1, 6.6 and 8.1 $Å^{-1}$. The quantitative results derived from the LCF confirmed a decrease in the $NiMgO_X$ fraction to 49 % when cooling down in reaction mixture to 600 °C. At the same time, the share of Ni maintained in the metallic and active state is 23 %. Finally, the lowest $NiMgO_X$ fraction was measured for the catalyst cooled down to room temperature in the SRM gas mixture, with 25 % $NiMgO_X$, 49 % metallic Ni and 26 % NiO at the end of the subsequent light-off/light-out cycle. However, despite this approach allows to preserve most of the Ni species in their reduced and active form and to minimize Ni oxidation and incorporation in mixed oxides, it poses environmental concerns due to CH_4 slips that occurs once the reactor temperature and CH_4 conversion drop. Furthermore, as previously shown in this section (black curve in Fig. 8b), switching from RM to N_2 at 600 °C is effective in upholding some active sites, as the resulting 15Ni/MG70 sample converts CH_4 above 550 °C. Thus, this adjusted shut-down procedure allows to maintain a partially active state even for the 15Ni/MG70, a monometallic Ni-based sample with relatively high Mg:Al ratio and intrinsically more sensitive to water vapor. As demonstrated by our activity data, after such a reactor shut-down protocol the catalyst reactivation is possible without the use of pure hydrogen by just heating up the catalyst bed in RM.

3.7. Catalyst reactivation investigated by in situ/operando XAS and XRD

To complement the *in situ* XAS and XRD investigations reported in Section 3.5, which were performed during the simulated reactor shut-down in 2 vol% H_2O/N_2, additional *operando* measurements were conducted for the mono- and bimetallic catalysts during the subsequent light-off in RM. These experiments focused on assessing the residual activity and, particularly, on evaluating the catalyst reactivation ability. Since the 15Ni/MG70 sample showed no activity recovery during the laboratory tests (Fig. 7b) after exposure to H_2O/N_2, this sample was excluded from these investigations.

The results of the LCF analysis of the *operando* XANES spectra collected at Ni K edge during the light-off in RM are displayed in Fig. 12, together with the simultaneously recorded methane conversion profiles. Complete methane conversion was achieved for all studied catalysts during the SRM light-off. The reaction onset occurred at 435 °C for 15Ni/MG28, while for both bimetallic catalysts methane conversion started between 335 and 340 °C (Figure S37). At the reaction onset, the fractions of metallic Ni were 5 %, 56 % and 29 % for 15Ni/MG28, 15Ni1Pt/MG28, and 15Ni1Pt/MG70, respectively. These values are in line with the Ni speciation at the end of the simulated shut-down procedure (Fig. 10b-d). As the temperature increased during the SRM light-off, Ni reduction was observed in all catalysts. This process was sustained by the simultaneous increase in CH_4 conversion. For the 15Ni/MG28 sample, the reduction of Ni species was noticed only after CH_4 conversion exceeded 25 %, while for the two Pt-promoted catalysts the formation of metallic Ni was already pronounced at low (<10 %) CH_4 conversion. These results suggest that Ni species in the latter catalysts exhibit higher reducibility, which could be endorsed by the hydrogen spillover process from Pt [27,30]. At the end of the light-off, *i.e.,* at 900 °C, the fraction of metallic Ni follows the order 15Ni1Pt/MG28 (92 %)> 15Ni1Pt/MG70 (76 %)> 15Ni/MG28 (62 %) which aligns well with the catalyst starting state (at the reaction onset) and the observed stability of these samples during the tests described in Sections 3.3 and 3.4.

Once the highest temperature of 900 °C was reached, further reduction of Ni^{2+} species to metallic Ni was observed in all catalysts according to the LCF of the XANES Ni K edge spectra collected while holding the temperature constant for 10 min (Figure S38). As a result of this procedure, all the catalysts contained over 75 % metallic Ni (96 % in 15Ni1Pt/MG28, 85 % in 15Ni/MG28, and 79 % in 15Ni1Pt/MG70). The 15Ni1Pt/MG70 catalyst was the only one still containing a small amount of $NiMgO_X$, despite its concentration decreased during light-off and holding time at 900 °C. The observed behavior shows that, owing to the low Pt loading, its ability to facilitate Ni reduction does not impact all Ni species in the catalyst. Complementary *operando* XRD data (Figure S39) confirmed the recovery of the metallic Ni phase during the SRM light-off, which was easier to achieve in the Pt-promoted catalysts. In particular, the growth of the Ni *fcc* (200) reflection is observed above 650 °C for 15Ni1Pt/MG28, while only above 800 °C for 15Ni1Pt/MG70. The absence of ordered Ni phases in the monometallic 15Ni/MG28 catalyst is most likely due to the lower fraction of metallic Ni at the end of the experiment.

All in all, the positive effects of Pt and the lower Mg:Al ratio on the activity and stability of Ni-based catalysts could be ascribed to the higher fraction of metallic Ni present in these materials. Based on the *in situ/operando* XAS and XRD investigations conducted in this study, these features were also found to facilitate catalyst reactivation by reduction of Ni species under transient reaction conditions.

4. Conclusions

In this study, the catalyst composition was adjusted for Ni-based mono- and bimetallic catalysts for steam reforming of methane with the aim of improving catalyst stability during dynamic daily start-up and shut-down operation, as encountered in small-scale reformers. Starting from different hydrotalcite-derived supports, MG28 and MG70, two Mg:

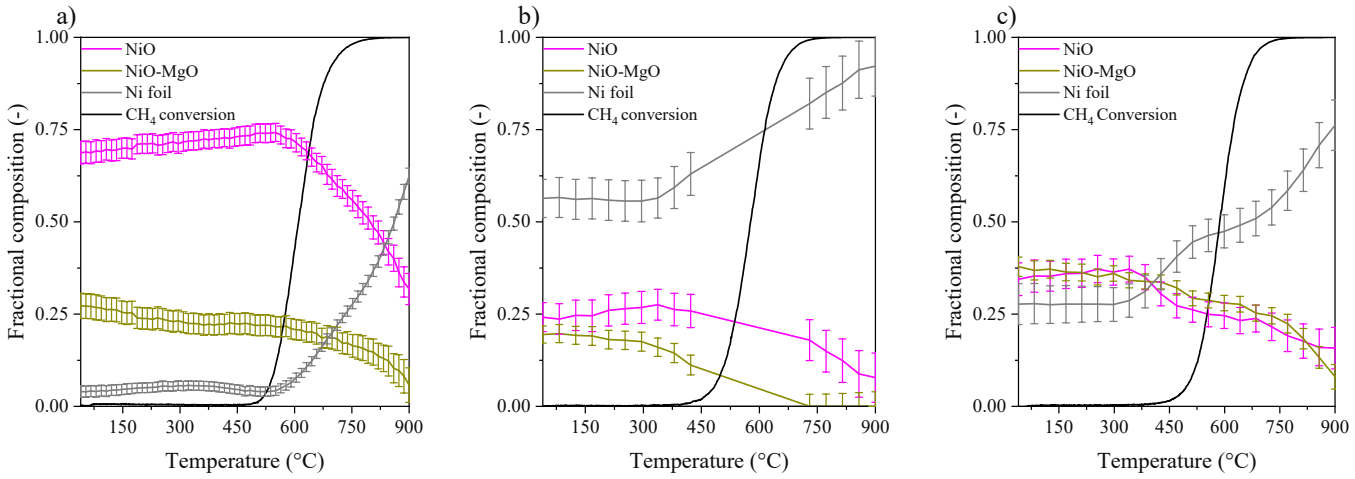

Fig. 12. Results from LCF of *operando* XANES at Ni K edge during heating up in RM after deactivation in H_2O-saturated inert for (a) 15Ni/MG28, (b) 15Ni1Pt/MG28 and (c) 15Ni1Pt/MG70, together with the corresponding CH_4 conversion data. Pt L_3 edge data for the two bimetallic catalysts show that Pt remains in reduced state during the same procedure.

Al ratios (0.5 and 3) were used for the preparation of the Ni- and Ni-Pt catalysts. The resulting samples were thoroughly tested and characterized in their calcined and reduced state. The catalyst structure was monitored during dynamic and severe reaction conditions up to 900 °C using *in situ* and *operando* methods. Particular focus was laid on the effect of the reactor shut-down procedure on the catalyst structure and deactivation/reactivation behavior.

The impact of the Mg:Al ratio was already observed in the structure of the freshly prepared catalysts. According to the electron microscopy and *ex situ* XAS investigations, the incorporation of Ni into MgO lattice is promoted by high Mg:Al ratios, which results in the formation of hardly reducible $NiMgO_X$ species. The analysis of the *in situ/operando* XAS and XRD data acquired during catalyst pre-reduction and SRM confirmed that Pt presence promotes the reduction of both NiO and $NiMgO_X$, and contributes to an early reaction onset for the calcined or pre-reduced Ni-Pt catalysts. Systematic activity tests identified the highest SRM performance accompanied by the ability to auto-activate for the Ni-Pt/MG28 catalyst. This sample was as well the most robust during various reactor shut-down procedures.

Overall, the following insights were obtained for the monometallic Ni and bimetallic Ni-Pt samples: (i) trace amounts of water contribute to Ni oxidation in the absence of/at low CH_4 conversion, and the related catalyst deactivation extent scales with increasing temperature under such conditions, (ii) Pt addition and/or a low Mg:Al ratio represent effective strategies to mitigate catalyst deactivation during reactor shut-down, (iii) the use of Pt-promoted bimetallic catalysts in case of prolonged exposure to water vapor at high temperatures is beneficial for retaining the catalytic activity without the need of further reduction steps before resuming operation. Finally, an optimized reactor shut-down procedure was identified, consisting in cooling down the catalyst bed in SRM gas mixture close to the reaction extinction temperature (600 °C), and only then flushing the reactor with inert gas while further cooling to ambient temperature. This protocol allows to maintain the catalyst in a partially active state even in the absence of a noble metal promoter and for high Mg:Al ratios in the carrier material. Furthermore, as shown by the *operando* XAS data, the subsequent catalyst reactivation entailing substantial Ni reduction is possible in reaction mixture without the use of pure hydrogen. In general, these findings provide a better understanding of the catalyst structural dynamics under transient reaction conditions and facilitate a knowledge-driven design of improved catalysts and optimized reactor operation protocols.

CRediT authorship contribution statement

Maria Casapu: Writing – review & editing, Visualization, Validation, Supervision, Project administration, Methodology, Investigation, Funding acquisition, Conceptualization. **Solenn Reguer:** Writing – review & editing, Validation, Software, Methodology. **Jan-Dierk Grunwaldt:** Writing – review & editing, Visualization, Validation, Supervision, Resources, Project administration, Funding acquisition, Conceptualization. **Radian Popescu:** Writing – review & editing, Visualization, Validation, Formal analysis, Data curation. **Andrea De Giacinto:** Writing – original draft, Visualization, Methodology, Investigation, Formal analysis, Data curation. **Dmitry E. Doronkin:** Writing – review & editing, Visualization, Validation, Investigation. **Enrico Tusini:** Visualization, Validation, Formal analysis, Data curation.

Declaration of Competing Interest

The authors declare that they have no known competing financial interests or personal relationships that could have appeared to influence the work reported in this paper.

Acknowledgements

This work was funded by the European Union's Horizon 2020 Research and Innovation program under the Marie Sklodowska-Curie Actions — Innovative Training Network (MSCA-ITN) grant agreement 813748 (BIKE Project). We acknowledge DESY (Hamburg, Germany), a member of the Helmholtz Association HGF, for the provision of experimental facilities. Parts of this research were carried out at PETRA III. Data was collected using beamline P65 operated by DESY Photon Science. We would like to thank Dr. S. Levcenko and Dr. E. Welter for assistance during the experiments. Beamtime was allocated for proposal II-20230692. We acknowledge SOLEIL for the provision of synchrotron radiation facilities, and thank the whole DiffAbs beamline staff, and especially Dr. C. Mocuta for assistance in using the DiffAbs beamline (proposals 20221619 and 20231744). We would like to thank Sasol Germany GmBH for providing the precursors of the support materials. The authors would like to thank Dr. A. Sapronov, Dr. T. J. Eldridge, Dr. M. Kurt, Dr. S.-L. Heck, Dr. V. Marchuk, Dr. S. Struzek and L. Baumgarten (KIT) for beamtime support. Dr. T. Bergfeldt (IAM-AWP, KIT) is acknowledged for ICP-OES measurements. S. Kurukunda and J. Pesek (ITCP, KIT) are acknowledged for N_2 physisorption measurements and technical support, respectively. Dr. X. T. Nguyen (ICCOM-Pisa) is acknowledged for performing the thermodynamic equilibrium

simulations. The Laboratory for Electron Microscopy (KIT) is acknowledged for electron microscopy investigations.

Appendix A. Supporting information

Supplementary data associated with this article can be found in the online version at doi:10.1016/j.apcatb.2025.126305.

Data availability

The data that support the findings of this study is available on the KITopen platform at 10.35097/qf2d3fahq22q5hjx.

References

[1] J.R. Rostrup-Nielsen, Catalytic Steam Reforming, in: M.B. John, R. Anderson (Eds.), Catal. Sci. Technol., Springer, Berlin, Heidelberg, 1984, pp. 1–117, https://doi.org/10.1007/978-3-642-93247-2_1.

[2] J.R. Rostrup-Nielsen, 40 years in catalysis, Catal. Today 111 (2006) 4–11, https://doi.org/10.1016/j.cattod.2005.10.016.

[3] J.R. Rostrup-Nielsen, Syngas in perspective, Catal. Today 71 (2002) 243–247, https://doi.org/10.1016/S0920-5861(01)00454-0.

[4] I. Dincer, C. Acar, Review and evaluation of hydrogen production methods for better sustainability, Int. J. Hydrogen Energy 40 (2015) 11094–11111, https://doi.org/10.1016/j.ijhydene.2014.12.035.

[5] Global Hydrogen Review 2025, Int. Energy Agency (2025). ⟨https://www.iea.org/reports/global-hydrogen-review-2025⟩ (accessed October 30, 2025).

[6] I. Dincer, Green methods for hydrogen production, Int. J. Hydrogen Energy 37 (2012) 1954–1971, https://doi.org/10.1016/J.IJHYDENE.2011.03.173.

[7] R. Yukesh Kannah, S. Kavitha, Preethi, O. Parthiba Karthikeyan, G. Kumar, N. V. Dai-Viet, J. Rajesh Banu, Techno-economic assessment of various hydrogen production methods – a review, Bioresour. Technol. 319 (2021) 124175, https://doi.org/10.1016/j.biortech.2020.124175.

[8] G.M.C. Jiefeng Lin, Catalyst for high temperature steam reforming, US10010876B2 (2016). ⟨https://patents.google.com/patent/US10010876B2/⟩.

[9] J.R. Rostrup-Nielsen, Process for the catalytic steam reforming of hydrocarbons, US3926583A (1975). ⟨https://patents.google.com/patent/US3926583A/⟩.

[10] C.V.O. Joachim Harteg Jacobsen, C. Daugaard, steam reforming catalyst and method of preparation, US9789470B2 (2017). ⟨https://patents.google.com/patent/US9789470B2/⟩.

[11] S. Saeedi, X.T. Nguyen, F. Bossola, C. Evangelisti, V. Dal Santo, Methane reforming processes: advances on mono- and bimetallic Ni-based catalysts supported on Mg-Al mixed oxides, Catalysts 13 (2023) 379, https://doi.org/10.3390/catal13020379.

[12] Z. Boukha, C. Jiménez-González, B. de Rivas, J.R. González-Velasco, J.I. Gutiérrez-Ortiz, R. López-Fonseca, Synthesis, characterisation and performance evaluation of spinel-derived Ni/Al_2O_3 catalysts for various methane reforming reactions, Appl. Catal. B Environ. 158–159 (2014) 190–201, https://doi.org/10.1016/J.APCATB.2014.04.014.

[13] U. Sikander, S. Sufian, M.A. Salam, A review of hydrotalcite based catalysts for hydrogen production systems, Int. J. Hydrogen Energy 42 (2017) 19851–19868, https://doi.org/10.1016/J.IJHYDENE.2017.06.089.

[14] D. Li, Y. Nakagawa, K. Tomishige, Methane reforming to synthesis gas over Ni catalysts modified with noble metals, Appl. Catal. A Gen. 408 (2011) 1–24, https://doi.org/10.1016/j.apcata.2011.09.018.

[15] Y.S. Park, M. Kang, P. Byeon, S.Y. Chung, T. Nakayama, T. Ko, H. Hwang, Fabrication of a regenerable Ni supported NiO-MgO catalyst for methane steam reforming by exsolution, J. Power Sources 397 (2018) 318–324, https://doi.org/10.1016/j.jpowsour.2018.07.025.

[16] J.E. Min, Y.J. Lee, H.G. Park, C. Zhang, K.W. Jun, Carbon dioxide reforming of methane on Ni–MgO–Al_2O_3 catalysts prepared by sol–gel method: effects of Mg/Al ratios, J. Ind. Eng. Chem. 26 (2015) 375–383, https://doi.org/10.1016/J.JIEC.2014.12.012.

[17] S. Narayanan, G. Sreekanth, Problems involved in the reducibility of the NiO–MgO system as evidenced by X-ray diffraction, electron paramagnetic resonance, electron spectroscopy for chemical analysis and adsorption techniques, J. Chem. Soc. Faraday Trans. 89 (1993) 943–949, https://doi.org/10.1039/FT9938900943.

[18] Y.H. Wang, H.M. Liu, B.Q. Xu, Durable Ni/MgO catalysts for CO_2 reforming of methane: activity and metal–support interaction, J. Mol. Catal. A Chem. 299 (2009) 44–52, https://doi.org/10.1016/J.MOLCATA.2008.09.025.

[19] M.M. Danilova, Z.A. Fedorova, V.I. Zaikovskii, A.V. Porsin, V.A. Kirillov, T. A. Krieger, Porous nickel-based catalysts for combined steam and carbon dioxide reforming of methane, Appl. Catal. B Environ. 147 (2014) 858–863, https://doi.org/10.1016/J.APCATB.2013.10.005.

[20] M. Yu, K. Zhu, Z. Liu, H. Xiao, W. Deng, X. Zhou, Carbon dioxide reforming of methane over promoted $Ni_xMg_{1-x}O$ (111) platelet catalyst derived from solvothermal synthesis, Appl. Catal. B Environ. 148–149 (2014) 177–190, https://doi.org/10.1016/j.apcatb.2013.10.046.

[21] R.K. Singha, A. Yadav, A. Agrawal, A. Shukla, S. Adak, T. Sasaki, R. Bal, Synthesis of highly coke resistant Ni nanoparticles supported MgO/ZnO catalyst for reforming of methane with carbon dioxide, Appl. Catal. B Environ. 191 (2016) 165–178, https://doi.org/10.1016/J.APCATB.2016.03.029.

[22] F. Joensen, J.R. Rostrup-Nielsen, Conversion of hydrocarbons and alcohols for fuel cells, J. Power Sources 105 (2002) 195–201, https://doi.org/10.1016/S0378-7753(01)00939-9.

[23] S. Ahmed, M. Krumpelt, Hydrogen from hydrocarbon fuels for fuel cells, Int. J. Hydrogen Energy 26 (2001) 291–301, https://doi.org/10.1016/S0360-3199(00)00097-5.

[24] E. Davies, A. Ehrmann, E. Schwenzfeier-Hellkamp, Safety of hydrogen storage technologies, Processes 12 (2024) 2182, https://doi.org/10.3390/pr12102182.

[25] T. Ohi, T. Miyata, D. Li, T. Shishido, T. Kawabata, T. Sano, K. Takehira, Sustainability of Ni loaded Mg–Al mixed oxide catalyst in daily startup and shutdown operations of CH_4 steam reforming, Appl. Catal. A Gen. 308 (2006) 194–203, https://doi.org/10.1016/j.apcata.2006.04.025.

[26] I.H. Son, S.J. Lee, A. Soon, H.S. Roh, H. Lee, Steam treatment on Ni/γ-Al_2O_3 for enhanced carbon resistance in combined steam and carbon dioxide reforming of methane, Appl. Catal. B Environ. 134–135 (2013) 103–109, https://doi.org/10.1016/J.APCATB.2013.01.001.

[27] E. Tusini, M. Casapu, A. Zimina, D.E. Doronkin, H. Störmer, L. Barthe, S. Belin, J.-D. Grunwaldt, Structural changes of Ni and Ni–Pt methane steam reforming catalysts during activation, reaction, and deactivation under dynamic reaction conditions, ACS Catal. 14 (2024) 7463–7477, https://doi.org/10.1021/acscatal.3c05847.

[28] D. Li, I. Atake, T. Shishido, Y. Oumi, T. Sano, K. Takehira, Self-regenerative activity of Ni/Mg(Al)O catalysts with trace Ru during daily start-up and shut-down operation of CH_4 steam reforming, J. Catal. 250 (2007) 299–312, https://doi.org/10.1016/J.JCAT.2007.06.002.

[29] T.-Y. Kim, J.-H. Lee, S. Jo, J. Kim, J.-H. Woo, R. Dhanusuraman, J.-C. Kim, S.-C. Lee, Improving the stability of Ru-doped Ni-based catalysts for steam methane reforming during daily startup and shutdown operation, Catalysts 13 (2023) 949, https://doi.org/10.3390/catal13060949.

[30] T. Miyata, D. Li, M. Shiraga, T. Shishido, Y. Oumi, T. Sano, K. Takehira, Promoting effect of Rh, Pd and Pt noble metals to the Ni/Mg(Al)O catalysts for the DSS-like operation in CH_4 steam reforming, Appl. Catal. A Gen. 310 (2006) 97–104, https://doi.org/10.1016/J.APCATA.2006.05.022.

[31] Y. Zhan, D. Li, K. Nishida, T. Shishido, Y. Oumi, T. Sano, K. Takehira, Preparation of "intelligent" Pt/Ni/Mg(Al)O catalysts starting from commercial Mg–Al LDHs for daily start-up and shut-down steam reforming of methane, Appl. Clay Sci. 45 (2009) 147–154, https://doi.org/10.1016/J.CLAY.2009.05.002.

[32] U.E.S. Amjad, C.W.M. Quintero, G. Ercolino, C. Italiano, A. Vita, S. Specchia, Methane steam reforming on the Pt/CeO_2 catalyst: effect of daily start-up and shut-down on long-term stability of the catalyst, Ind. Eng. Chem. Res. 58 (2019) 16395–16406, https://doi.org/10.1021/ACS.IECR.9B02436.

[33] D. Li, K. Nishida, Y. Zhan, T. Shishido, Y. Oumi, T. Sano, K. Takehira, Superior catalytic behavior of trace Pt-doped Ni/Mg(Al)O in methane reforming under daily start-up and shut-down operation, Appl. Catal. A Gen. 350 (2008) 225–236, https://doi.org/10.1016/j.apcata.2008.08.017.

[34] C. Vogt, J. Kranenborg, M. Monai, B.M. Weckhuysen, Structure sensitivity in steam and dry methane reforming over nickel: activity and carbon formation, ACS Catal. 10 (2019) 1428–1438, https://doi.org/10.1021/ACSCATAL.9B04193.

[35] A. Braga, M. Armengol-Profitós, L. Pascua-Solé, X. Vendrell, L. Soler, I. Serrano, I. J. Villar-Garcia, V. Pérez-Dieste, N.J. Divins, J. Llorca, Bimetallic NiFe nanoparticles supported on CeO_2 as catalysts for methane steam reforming, ACS Appl. Nano Mater. 6 (2023) 7173–7185, https://doi.org/10.1021/ACSANM.3C00104.

[36] D. Liu, Y. Li, M. Kottwitz, B. Yan, S. Yao, A. Gamalski, D. Grolimund, O. V. Safonova, M. Nachtegaal, J.G. Chen, E.A. Stach, R.G. Nuzzo, A.I. Frenkel, Identifying dynamic structural changes of active sites in Pt–Ni bimetallic catalysts using multimodal approaches, ACS Catal. 8 (2018) 4120–4131, https://doi.org/10.1021/ACSCATAL.8B00706.

[37] D. Eggart, A. Zimina, G. Cavusoglu, M. Casapu, D.E. Doronkin, K.A. Lomachenko, J.-D. Grunwaldt, Versatile and high temperature spectroscopic cell for operando fluorescence and transmission x-ray absorption spectroscopic studies of heterogeneous catalysts, Rev. Sci. Instrum. 92 (2021) 23106, https://doi.org/10.1063/5.0038428.

[38] S. Brunauer, P.H. Emmett, E. Teller, Adsorption of gases in multimolecular layers, J. Am. Chem. Soc. 60 (1938) 309–319, https://doi.org/10.1021/ja01269a023.

[39] C.A. Schneider, W.S. Rasband, K.W. Eliceiri, NIH Image to ImageJ: 25 years of image analysis, Nat. Methods 9 (2012) 671–675, https://doi.org/10.1038/nmeth.2089.

[40] Jems-Swiss, (n.d.). ⟨https://www.jems-swiss.ch/⟩ (accessed December 8, 2025).

[41] K. Hou, R. Hughes, The kinetics of methane steam reforming over a Ni/α-Al_2O_3 catalyst, Chem. Eng. J. 82 (2001) 311–328, https://doi.org/10.1016/S1385-8947(00)00367-3.

[42] B. Ravel, M. Newville, ATHENA, ARTEMIS, HEPHAESTUS: Data analysis for X-ray absorption spectroscopy using IFEFFIT, J. Synchrotron Radiat. 12 (2005) 537–541, https://doi.org/10.1107/S0909049505012719.

[43] B. Ravel, Quantitative EXAFS Analysis 1 (2016).

[44] K. Desjardins, C. Mocuta, A. Dawiec, S. Réguer, P. Joly, J.M. Dubuisson, F. Alves, A. Noureddine, F. Bompard, D. Thiaudière, The CirPAD, a circular 1.4 M hybrid pixel detector dedicated to X-ray diffraction measurements at Synchrotron SOLEIL, J. Synchrotron Radiat. 29 (2022) 180–193, https://doi.org/10.1107/S1600577521012492.

[45] F. Arena, A. Licciardello, A. Parmaliana, The role of Ni^{2+} diffusion on the reducibility of NiO/MgO system: a combined TRP-XPS study, Catal. Lett. 6 (1990) 139–149, https://doi.org/10.1007/BF00764063.

[46] A. Parmaliana, F. Arena, F. Frusteri, N. Giordano, Temperature-programmed reduction study of NiO–MgO interactions in magnesia-supported Ni catalysts and

NiO–MgO physical mixture, J. Chem. Soc. Faraday Trans. 86 (1990) 2663–2669, https://doi.org/10.1039/FT9908602663.
[47] J.D. Grunwaldt, A.M. Molenbroek, N.Y. Topsøe, H. Topsøe, B.S. Clausen, In situ investigations of structural changes in Cu/ZnO catalysts, J. Catal. 194 (2000) 452–460, https://doi.org/10.1006/JCAT.2000.2930.
[48] S. Pöyhtäri, J. Ruokoja, E.-P. Heikkinen, A. Heikkilä, T. Kokkonen, P. Tynjälä, Kinetic analysis of hydrogen reduction of nickel compounds, Metall. Mater. Trans. B 55 (2024) 251–265, https://doi.org/10.1007/s11663-023-02955-6.
[49] K. Okumura, H. Hoshi, H. Iiyoshi, H. Takaba, Formation of a Pt–MgO solid solution: analysis by X-ray absorption fine structure spectroscopy, ACS Omega 7 (2022) 27458–27468, https://doi.org/10.1021/acsomega.2c02486.
[50] K. Asakura, H. Nagahiro, N. Ichikuni, Y. Iwasawa, Structure and catalytic combustion activity of atomically dispersed Pt species at MgO surface, Appl. Catal. A Gen. 188 (1999) 313–324, https://doi.org/10.1016/S0926-860X(99)00247-1.
[51] T. Tanabe, Y. Nagai, K. Dohmae, H. Sobukawa, H. Shinjoh, Sintering and redispersion behavior of Pt on Pt/MgO, J. Catal. 257 (2008) 117–124, https://doi.org/10.1016/J.JCAT.2008.04.012.
[52] J.I. Langford, A.J.C. Wilson, IUCr, Scherrer after sixty years: a survey and some new results in the determination of crystallite size, J. Appl. Cryst. 11 (1978) 102–113, https://doi.org/10.1107/S0021889878012844.
[53] C. Di Valentin, L. Giordano, G. Pacchioni, N. Rösch, Nucleation and growth of Ni clusters on regular sites and F centers on the MgO(001) surface, Surf. Sci. 522 (2003) 175–184, https://doi.org/10.1016/S0039-6028(02)02344-0.
[54] G. Wang, Y. Xu, P. Qian, Structural characteristics and thermal stability of Pt-Ni nanoparticles, Appl. Phys. A 129 (2023) 105, https://doi.org/10.1007/s00339-022-06381-4.
[55] I.M.S. Anekwe, S.O. Akpasi, E.M. Enemuo, D. Ashiegbu, S.I. Mustapha, Y.M. Isa, Innovations in catalytic understanding: a journey through advanced characterization, Mater. Today Catal. 7 (2024) 100061, https://doi.org/10.1016/J.MTCATA.2024.100061.
[56] S. Kim, E. Sasmaz, Transformation of platinum single-atom catalysts to single-atom alloys on supported nickel: TEM and XAS spectroscopic investigation, ChemCatChem 14 (2022) e202200568, https://doi.org/10.1002/cctc.202200568.
[57] B. Moraweck, A.J. Renouprez, E.K. Hlil, R. Baudoing-Savois, Alloying effects on x-ray absorption edges in nickel-platinum single crystals, J. Phys. Chem. 97 (1993) 4288–4292, https://doi.org/10.1021/j100119a009.
[58] L. Li, L. Zhou, S. Ould-Chikh, D.H. Anjum, M.B. Kanoun, J. Scaranto, M.N. Hedhili, S. Khalid, P.V. Laveille, L. D'Souza, A. Clo, J.M. Basset, Controlled surface segregation leads to efficient coke-resistant nickel/platinum bimetallic catalysts for the dry reforming of methane, ChemCatChem 7 (2015) 819–829, https://doi.org/10.1002/CCTC.201402965.
[59] A. Sadezky, H. Muckenhuber, H. Grothe, R. Niessner, U. Pöschl, Raman microspectroscopy of soot and related carbonaceous materials: spectral analysis and structural information, Carbon N.Y. 43 (2005) 1731–1742, https://doi.org/10.1016/J.CARBON.2005.02.018.
[60] R. Sainju, D. Rathnayake, H. Tan, G. Bollas, A.M. Dongare, S.L. Suib, Y. Zhu, In situ studies of single-nanoparticle-level nickel thermal oxidation: from early oxide nucleation to diffusion-balanced oxide thickening, ACS Nano 16 (2022) 6468–6479, https://doi.org/10.1021/acsnano.2c00742.
[61] J.G. Railsback, A.C. Johnston-Peck, J. Wang, J.B. Tracy, Size-dependent nanoscale kirkendall effect during the oxidation of nickel nanoparticles, ACS Nano 4 (2010) 1913–1920, https://doi.org/10.1021/NN901736Y.